

Article

# Advanced Structural Analysis of Innovative Steel–Glass Structures with Respect to the Architectural Design

Faham Tahmasebinia <sup>1,\*</sup>, Youtian Wang <sup>1</sup>, Siyuan Wu <sup>1</sup>, Justin Ho <sup>1</sup>, Weijia Shen <sup>1</sup>, Hongyi Ma <sup>2</sup>, Samad M. E. Sepasgozar <sup>3</sup>  and Fernando Alonso Marroquin <sup>1</sup>

<sup>1</sup> School of Civil Engineering, The University of Sydney, Sydney, NSW 2006, Australia; youtian.wang@sydney.edu.au (Y.W.); siwu4486@uni.sydney.edu.au (S.W.); juho6979@uni.sydney.edu.au (J.H.); wshe9631@uni.sydney.edu.au (W.S.); fernando.alonso@sydney.edu.au (F.A.M.)

<sup>2</sup> Faculty of Engineering, University of New South Wales, Sydney, NSW 2052, Australia; z5232399@zmail.unsw.edu.au

<sup>3</sup> Faculty of Arts, Design & Architecture, School of Built Environment, University of New South Wales, Sydney, NSW 2052, Australia; sepas@unsw.edu.au

\* Correspondence: faham.tahmasebinia@sydney.edu.au



**Citation:** Tahmasebinia, F.; Wang, Y.; Wu, S.; Ho, J.; Shen, W.; Ma, H.; Sepasgozar, S.M.E.; Marroquin, F.A. Advanced Structural Analysis of Innovative Steel–Glass Structures with Respect to the Architectural Design. *Buildings* **2021**, *11*, 208. <https://doi.org/10.3390/buildings11050208>

Academic Editors: Konstantinos Daniel Tsavdaridis, Gaochuang Cai and Amir Si Larbi

Received: 6 April 2021

Accepted: 6 May 2021

Published: 15 May 2021

**Publisher's Note:** MDPI stays neutral with regard to jurisdictional claims in published maps and institutional affiliations.



**Copyright:** © 2021 by the authors. Licensee MDPI, Basel, Switzerland. This article is an open access article distributed under the terms and conditions of the Creative Commons Attribution (CC BY) license (<https://creativecommons.org/licenses/by/4.0/>).

**Abstract:** This paper provides a comprehensive analysis of a steel–glass spindle torus structure based on the prototype of the Jewel Changi Airport, Singapore. Instead of studying a common cuboid building, the research in this paper focuses on a spindle torus shape structure which incorporates tremendous, curved members. Hence, the advanced modeling and structural analysis of this structure provides valuable information about an irregularly shaped building. Meanwhile, the modeling and analysis process of this innovative structure also gives rise to some practical design recommendations for both architects and engineers. In this paper, both global structure stability and local member buckling behavior were studied. With the use of commercial finite element software, Strand7 (R2.4.6) and ABAQUS (6.14), a series of numerical simulations were conducted. In terms of the behavior of the global structure, both numerical spindle torus models incorporating straight and curved steel members were tested under different load combinations specified in Australian building standards. A significant difference was observed between the results of the two models; therefore, research on the individual curved members was undertaken. Regarding the local member buckling behavior, the effective length factor for curved members with braced and sway boundaries conditions was investigated in Strand7. Moreover, the interaction curves of curved beams with different L/R ratios were compared with perfectly straight members in Australian building standards. ABAQUS can provide more precise predictions of local buckling behavior; therefore, the elastic local buckling behavior of the perimeter beams on different levels was investigated using ABAQUS. Additionally, the impacts of boundary conditions and L/R ratios on the beam buckling behavior are discussed.

**Keywords:** steel-glass structures; spindle torus structures; global structural performance; curved steel members; elastic buckling behavior of curved members

## 1. Introduction

### 1.1. Advantages of Steel–Glass Structures

Steel–glass structures are becoming increasingly popular in modern architecture. Over the past twenty years, a growing body of research and more widespread commercial use of innovative structures have been observed. As two materials which are often combined in the construction industry, steel and glass have been widely used in the roofs and facades of office buildings, residential buildings, and transport infrastructure [1]. During the assembly of steel–glass structures, the composite structure is first shaped by a steel or aluminum frame. Glass panels are then configured to fit the frame which forms the composite structure.

Steel–glass composite frames are advantageous compared with traditional steel frames. Firstly, the combined use of steel and glass diversifies the structural design. Compared with traditional steel structures with straight members, the irregular shapes of glass–steel structures allow designers to express their design concepts in more artistic ways, which improves the aesthetic value of the designed structure. By using different forms of surface coloring, printing, and processing, the properties of glass panels can be precisely customized. The variety of glass textures allows architects to design colorful urban landscapes with different design concepts [2]. Secondly, given the high transmittance and transparency of glass, steel–glass structures are also used to improve indoor illumination. For some commercial buildings such as fashion boutiques, steel–glass structures are often used in the fronts and interior to optimize the showcase setup and maximize indoor illumination. For public transport stations, glass–steel structures are widely used as railings [3]. Thirdly, due to improvements in manufacturing techniques, glass materials now possess a high degree of resistance to buckling and breakage. For instance, a laminated glass panel under axial load will exhibit high resistance to buckling, because all glass layers are mutually supported. If breakage occurs, the broken pieces of the glass panel will remain bonded together, exhibiting high residual stress [4].

### *1.2. Potential Applications of Steel–Glass Structures*

At present, innovative steel–glass structural designs have bright market prospects in the construction industry. In airports and railway stations, curved glass panels have been used with steel frames to form curved glass roofs [5]. The use of curved glass roofs not only improves indoor illumination, but also helps to control indoor temperatures. The same types of composite structures are also used in the roofs of museums and observation decks. In advanced applications of glass–steel structures, glass panels can be welded with steel beams to form glass–metal composites, which possess excellent load capacity under axial load [6]. In modern architecture, glass panels and steel supports are used to form steel-supported glass façades. For some temporary constructions, steel-supported glass façades can be used to replace concrete walls [1]. In the construction of skyscrapers, high-strength glass panels may be combined with steel frames to form high-performance curtain walls which act as the external façades of high-rise buildings.

### *1.3. Research Targets of the Numerical Analysis*

Although steel–glass composite structures have become more widely used in modern architecture, research regarding their overall loading performance is still limited. Therefore, it is necessary to conduct finite element modeling on innovative designs. Simulations of structural loading performance can be effectively used to validate existing design codes, providing valuable design recommendations for future designers. In this research, the global structural performance and local member behavior of a curved steel–glass spindle torus were studied. Instead of applying a theoretical structural model, the research investigated the loading performance of a curved glass spindle torus building structure at the Jewel Changi Airport in Singapore. Based on the research prototype, numerical models were developed in Strand7 and ABAQUS to analyze the structural behavior. Without internal support, an arced spindle torus can still span a considerable distance. However, a spindle torus with a long span may become unstable under the impacts of external load. This situation may be exacerbated by the presence of high compressive forces, imperfection effects, and other nonlinearity in the structure [7]. To investigate this structural instability, our numerical analysis of the curved spindle torus was divided into two sections: study of the behavior of the global structure, and an analysis of the behavior of the local member. The behavior of the global structure mainly includes displacement and stress within the steel structure. By regarding the wind load and live load as uniformly distributed load, the total displacement and fiber stress of the curved structure were analyzed. At the same time, the results from different solvers (linear and nonlinear) were compared. The local member behavior of the curved structure mainly includes the buckling behavior of each

steel member. In terms of the analysis results, the impacts of boundary conditions, member curvature, and other member properties to the buckling of the structural members were analyzed. The obtained results were compared with the calculation using AS4100 [8].

#### 1.4. Design Considerations and Costs of the Steel–Glass Structure

Curved steel structures are mainly designed to improve indoor illumination, spaciousness, and grandeur of public facilities. This design purpose results in a structural form with a large number of glass panels and arched supporting frames. Compared with other roof structures, curved steel–glass roofs do not lead to high costs. The additional cost induced by the curved steel frame can be counteracted by simplifying structural detailing, reducing flashing costs, and reducing vertex stitching for spans less than 25 m [9].

The roof cladding on curved roof beams usually does not require pre-bending, because most of the glass panels can directly fit into the curved roof during the installation. Although the curved appearance of the designed spindle torus can also be achieved by connecting multiple straight members, the design using straight members will incur a significant increase in the manufacturing cost. By contrast, a structural design using curved frames will be more cost-effective [9]. When designing the curved frame for a glass–steel structure, the boundary conditions of the glass panel should be determined first. Afterwards, a stable curved roof should be designed according to the membrane stiffness of glass panels. To maintain the stability of curved glass panels above the frame, it is necessary to avoid excessive bending of all glass panels. Hence, the “correct” geometry of all glass panels should be determined during the design phase to allow the membrane action due to the glass self-weight only [10].

#### 1.5. Active Research on Steel–Glass Structures

Regarding the active research on the steel glass structure, Richter [11] proposed the use of L-shape bounded joints to increase the lateral constraint for the glass panels and reduce the impacts of glass thickness on the behavior of the steel members. The linear elastic calculation can provide the appropriate and conservative capacity estimations in the architecture design when the steel–glass structure experiences suction load [12]. In addition, laminated glass is widely applied to steel–glass composite members [13]. Thus, it is suggested to use laminated glass in the innovative steel–glass structure because its higher stiffness can provide greater restraints than the conventional PVBs [14]. Additionally, the use of glass not only improves the aesthetic value of the proposed design but also works like the bracing members to provide lateral stability of the overall structure [15]. However, Bedon et al. [16] implemented state-of-the-art research on the mechanical behavior of steel glass façades under extreme loading conditions, including seismic and human-induced explosions. It was found that catastrophic failures tend to happen; therefore, it is necessary to design the steel–glass structure within the designed safety margin.

Curved beams are used as structural elements that have multiple applications in the construction field. They can be used in both bridge designs and light roof structures [17]. For a curved steel–glass structure and a straight steel–glass structure, the initial curvature is the only difference between the curved frame and the straight frame. Park [18] conducted pioneering systematic research of the torsional and distortional behavior of steel members induced by the initial curvature. Through extensive parametric studies, Park [18] produced a tentative design chart which relates the normal bending stress of the curved member to the spacing of intermediate diaphragm and ratio of distortional warping stress, which provides a new method to analyze the curved beam using various stress ratios instead of a single stress ratio. After that, Liu [19] studied the crashworthiness design of a curved steel beam with a thin-walled box section using the response surface method, and their work also proved the feasibility of predicting the mechanical performance of curved steel members.

Surprisingly, the presence of the initial curvature makes the behavior of curved beams much more complicated than straight beams [20]. The coupling of various deformations, when subjected to general loads, makes the behavior of curved beams complex. In the finite

element formula, this coupling effect makes it difficult to choose a suitable shape function to represent the strain field of the curved beam element [21]. Due to this mathematical complexity, most studies on the behavior of the curved beam are only concentrated on the linear analysis, and there are few nonlinear studies on the buckling of curved beams. For the curved beam under two special situations of uniform compression and uniform bending, Timoshenko [22] obtained critical load using the balance method, which did not consider the effect of warpage. Conventionally, curved beam analysts have adopted the assumptions of straight beams, for example, homogeneous and elastic materials, in-plane rigid cross-sections, large beam lengths compared to the cross-sectional dimensions, and negligible shear strain [23]. Vlasov's bending beam theory was accepted until Yoo proposed a new stability equation, which was analyzed by substituting the curvature term into the energy function and using a vibrational process [17]. Yang [21] pointed out that Vlasov and Yoo's theory is usually invalid because of an inconsistent analogy method. By contrast, Timoshenko's theory can only be used in the situation of solid beams, ignoring the effect of warpage [21].

Publications in the past three years analyzing the mainstream practices in this field were also studied. Firno et al. [24] assessed the bending performance of a novel composite solution for glass beams and evaluated major experimental outcomes from full-scale bending tests performed on I-shaped hybrid (HB) steel–glass beams. It involved a discussion for major experimental outcomes and comparative behaviors based on four full-scale prototypes, and measurement for strains and qualitative distribution of crack patterns. The combination of both the I-shaped hybrid (HB) and pre-stressing system of cables (PSHB) solutions can be a valid approach for the protection and safe control of glass structures. Gatheeshgar et al. [25] implemented experiments and applied finite element analysis to investigate the optimized flexural capacity of cold-formed steel (CFS) members. Compared with a commercially available lipped channel beam (LCB) with the same amount of material, the new cold-formed steel (CFS) sections possess the highest section moment capacity enhancements (up to 65%). Buchanan et al. [26] evaluated the current design provisions in EN 1993-1-4 (2015) and developed efficient and reliable design rules for stainless steel circular hollow section (CHS) beam-columns. It was found that the current European design guidance and the current design approach are conservative for members with a high ratio of bending moment to axial load, and the continuous strength method (CSM) can offer improvements over the current European guidance at the cross-sectional level. Zhang and Wang [27] provided a solution for free vibration and illustrated new results for elastically restrained functionally graded curved beams. A new model for elastically restrained functionally graded curved beams was also developed, and it was found that the Mori–Tanaka scheme is suitable for use on gradient microstructure with a discontinuous granule and high-blooded continuous matrix by considering interactions among adjoining inclusions. Yan et al. [28] conducted strength assessments for curved steel–concrete–steel (C-SCS) sandwich shells with bolt connectors under concentrated load. It was concluded that the ultimate strength of curved steel–concrete–steel (C-SCS) shells was improved with increasing concrete and face steel plate thicknesses and with decreasing shear connector spacing. The optimal rise–span ratio was found to be between 0.25 and 0.33. Additionally, a large number of studies had been conducted on curved structural steel members [27–33].

The aforementioned literature in this section provided valuable ideas for global structural integrity analysis and individual curved member analysis in this research. The global performance of the integrated spindle torus structure and level of safety analysis of the curved structural members will be further demonstrated in this paper.

## 2. Case Study

Jewel Changi Airport is an environmentally friendly landscape in Singapore [29]. In Singapore's Green Mark Program, Jewel Changi Airport achieved a platinum rating for its excellent ecological sustainability. The latest development project of Changi Airport, the construction of Jewel Changi was completed in 2019. The 1.7 million-square-foot

construction was located at the former parking lot of the airport. As the fourth terminal of Singapore Airport, Jewel Changi is connected with the other three terminals by train [30].

To achieve ideal aesthetic performance, the design team designed the glass-enclosed building with a toroidal shape. The Jewel Changi Airport has an elliptical toroid shape of around 200 m length and 150 m width. It is a continuous gridshell structure supported by 14 tree-like columns and several perimeter beams (ring beams). The structural design of the top of the glass-steel spindle torus is shown in Figure 1. At the top of the designed spindle torus, a central opening was configured. With the decoration of the internal forest valley and the indoor waterfall, the central opening of Jewel Changi Airport has become an attractive landscape for transiting passengers. The triangular panels made of steel and glass are used to discretize the shape. For the glass façade, 9000 high-performance glass panels were used. The glass panel was chosen because of its excellent transmittance, great energy efficiency, and low heat absorption under tropical climate. In Jewel Changi airport, the most fantastic attraction is named Rain Vortex, which is the tallest indoor waterfall in the world. With a height of 40 m, water flows from the central opening to a pool in the courtyard.

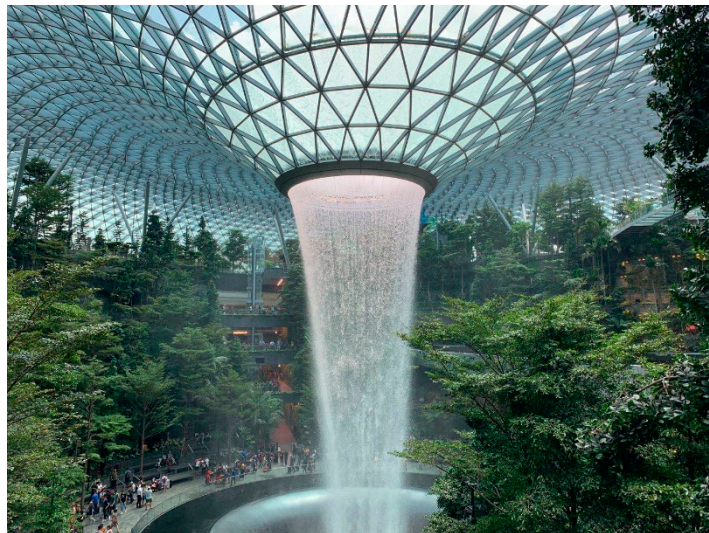


Figure 1. Central opening of Changi airport.

Conventional gridshell structures can be very thin, because they are only expected to resist in-plane compression and tension. However, the gridshell structure in the Jewel Changi Airport is required to accommodate both membrane forces in the shell and out-of-plane external forces which may bend the plane. To resist combined force on the gridshell structure, the design team estimated the forces in the shell and strengthened the structure at the bend position. The waterfall at the central opening dragged the grid-shell structure downwards, which added tension to the inner area of the perimeter beam. The surface tension of these membranes acts in two directions: hoop and meridian. These perimeter beams have a minimal bending moment and no risk of buckling behavior, so they are the shallowest members in the project, with a depth of only 8 inches. The forces exerted by the curvature are primarily compressive between the peripheral support, moving towards inner support. It has a compression hoop and meridian membrane force, which is similar to the spindle torus structure.

### 3. The Proposed Numerical Model and Modeling Details

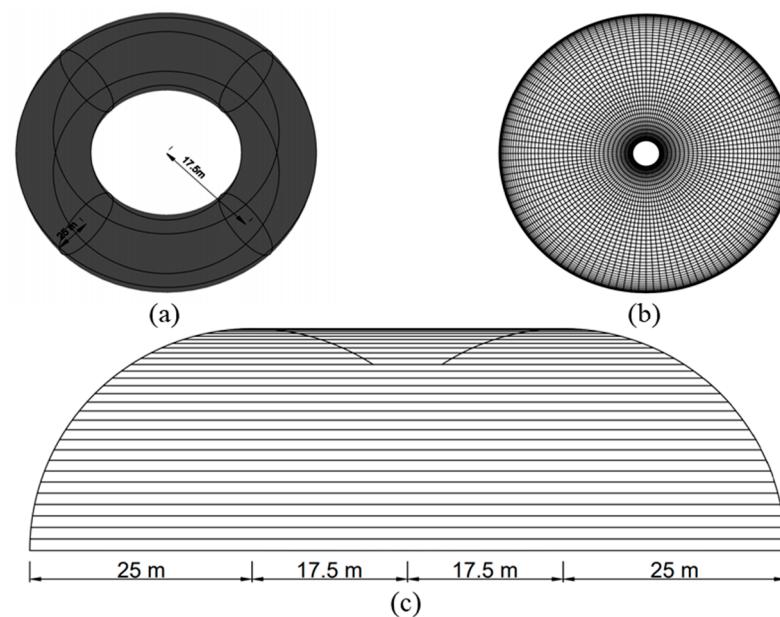
#### 3.1. Methodology

In this research, the loading performance of the glass spindle torus in Jewel Changi Airport was investigated using two numerical modeling packages, Strand7 and ABAQUS. The research methodology has exhibited high applicability on other case studies. With

these two powerful finite element modeling tools, the loading performance of other structures can also be captured by developing new structural models. At the first stage, two finite element models of the structure were developed using straight and curved beams in Strand7. The two developed models were subjected to five different load combinations in AS1170 [31], which included both strength limit state and serviceability limit state. The loading performance of the structure was simulated under both linear and non-linear solvers. Different from the linear solver, the nonlinear solver in Strand7 considers material and geometric nonlinearities when conducting finite element analysis. Instead of applying the load and displacement in one step, the nonlinear solver applies the prescribed displacement and load incrementally. This enables the impacts of geometrical imperfections (node defection) and material imperfections (nonlinear stress–strain relationship) to be accurately captured. However, in this research, only geometric nonlinearities were considered, because the elasticity of all structural members was assumed to be constant. When the designed structure was about to fail, the maximum fiber stress, displacement and deformed shape of the structure were recorded to analyze the structural failure modes. The simulated structural failure modes under different loads would identify the fragile sections of the innovative design, allowing future designers to reinforce similar structures contrapuntally. After investigating the structural global behaviors, the local member behaviors of the designed structure were also investigated. In Strand7, the longitudinal columns of the structure were loaded under axial compression until they buckled. The buckling load of the longitudinal columns with different curvature (L/R ratio) were compared with the elastic buckling load specified in AS1170 [31], helping select the maximum allowable column curvature. Meanwhile, the perimeter beams of the structure were subjected to the combined effect of axial load and in-plane bending until they buckled. The maximum compressive and bending capacity of the perimeter beams were demonstrated as an interaction curve, helping to determine the beam capacity under combined load. At the last stage, the buckling modes of perimeter beams at different levels of the structure were investigated using the buckle step in ABAQUS. After analyzing the buckling modes of perimeter beams at different levels, the effects of beam curvature and boundary conditions on the buckling load and shape were further investigated to determine an optimized beam design with high load capacity. After investigating the impacts of some key structural parameters, some practical design recommendations of the glass spindle torus, such as the recommended member curvature and boundary conditions, would be proposed by this research. This would be beneficial for the architectural design of similar structures; the designers could balance the aesthetic value and the loading performance of the structure using the recommended design parameters.

### *3.2. Schematic Model of the Target Structure*

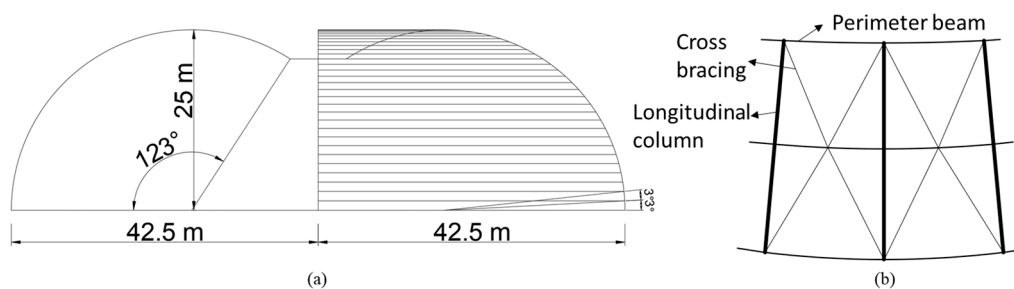
Based on the prototype (Jewel Changi Airport), a simplified finite element model was made. The model simplified the airport shape to a spindle torus. The toroid modelled had a circular cross-section radius of 25 m and a 17.5 m radius of the overall shape, as shown in Figure 2a,c. The circular toroid shape made analysis of the impact of a curved beam easier, due to its consistency of the L/R ratio in each level. The plan view of the model without the bracing element is shown in Figure 2b. Similar to the dome, torus consisted of multiple arches (bays) repeated and rotated along its central axis. The building standards AS4100 [8] and AS4600 [32] are only applied to straight design beams; therefore, two spindle torus structures incorporating curved and straight structural members were modeled for comparison.



**Figure 2.** Schematic design of the model ABAQUS: (a) isometric view; (b) top view; (c) front view.

This project only focused on the spindle torus shape structure. For the sake of simplification, the vertical columns and internal slabs were all removed. Correspondingly, in order to counteract the effect of eliminating the internal columns, the live load, which accounts for the external decoration such as glass, was reduced to the minimum (0.5 kPa) to reflect the true manifestation of the original complete structure. Moreover, besides some restraints to the external structure that the columns can provide, the vertical columns are mainly used to support the internal slabs and other decorations, which were not considered in this project.

The model consisted of 120 bays. A typical bay is shown in Figure 3b, each bay consisting of perimeter beams, cross bracings, and longitudinal columns. As shown in Figure 3a, 42 perimeter beams were placed 3 degrees or 1.309 m apart. Figure 3b shows a typical region of the structure, and it can be seen that the perimeter beams and longitudinal columns form the circular toroid shape, which is further supported by cross bracings. All elements chosen for this model are hollow sections that were produced according to the Onesteel manufacture guide [33]. These section properties are summarized in Table 1. The steel was assumed to be elastic-perfectly plastic with a nominal yield stress of 350 MPa. The section chosen for the perimeter beams was a  $250 \times 150 \times 9.0$  Rectangular Hollow Section. The section chosen for the cross bracings was a  $101.6 \times 3.2$  Circular Hollow Section. The section chosen for the longitudinal columns was a  $250 \times 250 \times 9.0$  Rectangular Hollow Section.

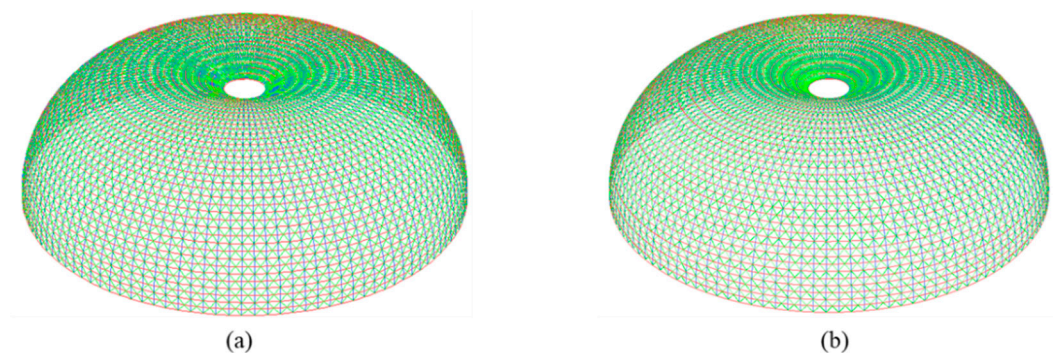


**Figure 3.** Schematic design of the model: (a) front view of the half-structure; (b) structural member demonstration.

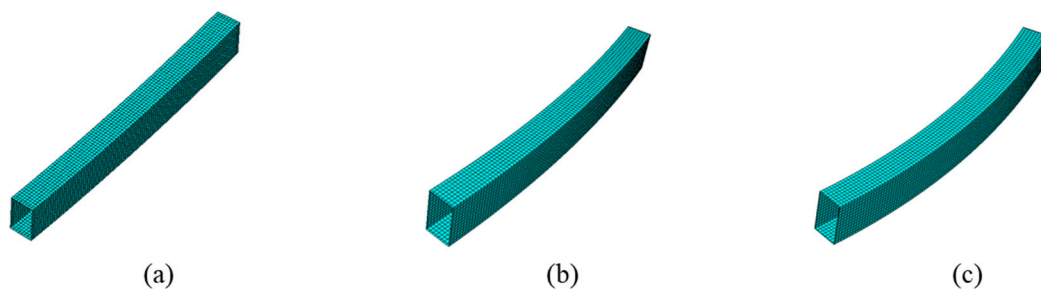
**Table 1.** Section property for different members.

	Perimeter Beams	Cross Bracing	Longitudinal Columns
Section name	250 × 150 × 9 RHS	101.6 × 3.2 CHS	250 × 250 × 9 RHS
Yield stress (MPa)	350	350	350
Section area (mm <sup>2</sup> )	6600	989.2	8400
Second moment area ( <i>x</i> -axis) (mm <sup>4</sup> )	$5.37 \times 10^7$	$1.199 \times 10^6$	$7.98 \times 10^7$
Second moment area ( <i>y</i> -axis) (mm <sup>4</sup> )	$2.43 \times 10^7$	$1.199 \times 10^6$	$7.98 \times 10^7$

Due to the complexity of the finite element model, the geometry of the model was initially sketched in AutoCAD and then imported into Strand7. Both curved and straight members were built for the model by conducting different numbers of subdivisions; these two models provided opportunities to study the global behavior of the structure. There was a high density of members; therefore, the difference between the two models with straight members and curved members could not be observed directly. The final visualization of finite element models in Strand7 is shown in Figure 4. Figure 4a represents the model in which two nodes are connected by one straight element directly, and Figure 4b represents the model in which there are 100 elements between two nodes; thus, the numerical model generated in Strand7 strictly followed the AutoCAD drawing with curved beam members.

**Figure 4.** Finite element models in Strand7: (a) the straight member model; (b) the curved member model.

For the local member buckling analysis, overall buckling of the curved member was conducted in Strand7 using the linear buckling solver, whereas the local buckling behaviors were analyzed in ABAQUS 6.14-1. In ABAQUS, the hollow sections are constructed by shell elements and analyzed by the linear perturbation procedure in buckle analysis. Some typical curved beam models are shown in Figure 5.

**Figure 5.** Finite element models in ABAQUS: (a) the perimeter beam on level 5; (b) the perimeter beam on level 15; (c) the perimeter beam on level 25.

### 3.3. Load Case Description

During daily use, the designed structure is expected to experience three types of loads, which include dead load, live load, and wind load. Assuming the designed roof is non-trafficable, the three types of loads can be introduced as follows according to AS1170.1 [31].

#### 3.3.1. Dead Load G

In this case, the dead load only accounts for the self-weight of all steel members. For simplification, the self-weight of all glass panels was regarded as a part of the vertical live load acting on the longitudinal columns. In the proposed design, the densities of all perimeter beams, longitudinal columns, and cross-bracings were assumed to be  $7850 \text{ kg/m}^3$ . The gravity load of all steel members was regarded as a uniformly distributed load acting vertically on each structural component. Using the linear static analysis in Strand7, the impacts of gravitational load were automatically simulated.

#### 3.3.2. Live Load Q

The live load on the designed structure mainly accounted for the self-weight of all glass panels. Due to the lightweight feature of the glass material, the imposed action of the glass cladding could be conservatively regarded as a face pressure of  $0.25 \text{ kPa}$ , referring to Table 3 in AS1170.1 [31]. At the medium height, the radius of the designed circle of the spindle torus was given as  $30 \text{ m}$ . The angle between each longitudinal column was  $3^\circ$ . Therefore, the average tributary width of each longitudinal column could be calculated as  $1.57 \text{ m}$ . With the average tributary width of longitudinal columns, the live load induced by glass panels could then be converted into a line load on the longitudinal column of approximately  $0.3925 \text{ kN/m}$ .

#### 3.3.3. Wind Load

The wind load subjected to the steel–glass structure was calculated based on both AS1170.2 [34] and Eurocode 1 [35]. The AS1170.2 [34] was used to estimate the design wind speed, and Eurocode 1 [35] was used to calculate the design wind pressure. Section 7.2.8 in Eurocode 1 [35] provides a specific wind pressure distribution for a dome roof, which is quite similar to the spindle torus structure in this project. However, unlike a rectangle section building with a dome roof structure, this steel–glass structure is a whole spindle torus shape structure. For simplification and out of conservative consideration, there were some adjustments made based on the calculation results from the standard. Firstly, the magnitude of the pressure force was assumed to be constant along with the height, and the perimeter beams were designed as the primary wind load-resisting members. Additionally, the wind pressure was estimated conservatively from the top of the structure ( $25 \text{ m}$ ). Secondly, the distribution of the force was slightly adjusted based on Figure 7.12 in Eurocode 1 [35]. Thirdly, the uniform distributed load (UDL) was calculated based on the mid-level longitudinal column spacing. The calculated values are displayed in Table 2.

**Table 2.** Wind loads on the structure.

Region	Windward Quarter	Sides	Leeward Quarter
Pressure (kPa)	+2.44	−4.82	−0.19
UDL (kN/m)	1.83	−3.615	−0.143

Note: The positive values mean the direction of the force is pointing inwards to the structure, whereas the negative values mean the direction of the force is pointing outwards of the structure, i.e., the suction effect.

#### 3.3.4. The Load Combinations

In addition to the individual load cases analysis, it was necessary to check the behavior of the structure under load combinations according to AS1170 [36].

Pedestrians will not have walking access on top of the structure; therefore, the steel glass structure was not designed for floor-type activities. Thus, according to Table 4.1 in AS1170 [31], the combination factor ( $\varphi_c$ ) should be equal to 0. Overall, there are three load

combinations and two load combinations needed to be considered for the strength limit state and serviceability limit state, respectively. These load combinations are described in Table 3.

**Table 3.** The linear load combinations.

	Strength Limit State	Serviceability Limit State
Load combinations	1.2G + 1.5Q 1.35G 1.2G + W	G + 0.7Q G + 0.7Q + W

### 3.4. The Expected Structural Deformation

An analysis was performed to predict the loading path and buckling shape using existing research. The model was a circular spindle toroid built with steel bracing and curved members, therefore the loading path was very similar to a circular dome.

To resist vertical load travelling along with the longitudinal columns, as shown in Figure 6a, the longitudinal column is not parallel to the vertical direction, which would cause an overturning moment on the base of the columns. This overturning moment causes axial force because the columns are “squishing” the perimeter beams, as shown in Figure 6b. This causes axial force in the perimeter beam called the hoop force, which is relevant to the expansion stability of the ring [37]. The hoop force resists the overturning moment; therefore, the hoop forces for the spindle torus will all be compression and the higher the perimeter beam is located, the higher the compressive hoop force.

Similar to the dome structure, due to the hoop force caused by the overturning [7], there are differences in the hoop force when it is near the top of the toroid. At the longitudinal column near the top of the toroid, the horizontal gap between the perimeter beams of adjacent levels is maximum. As a result, the bending in the columns is highest in the top of the toroid. If the vertical load is high enough, the perimeter beam will be in tension, having a tension hoop force. The hoop force will finally turn back to compression when it reaches the final few perimeter beams. The expected deformed shape is shown in Figure 6c.

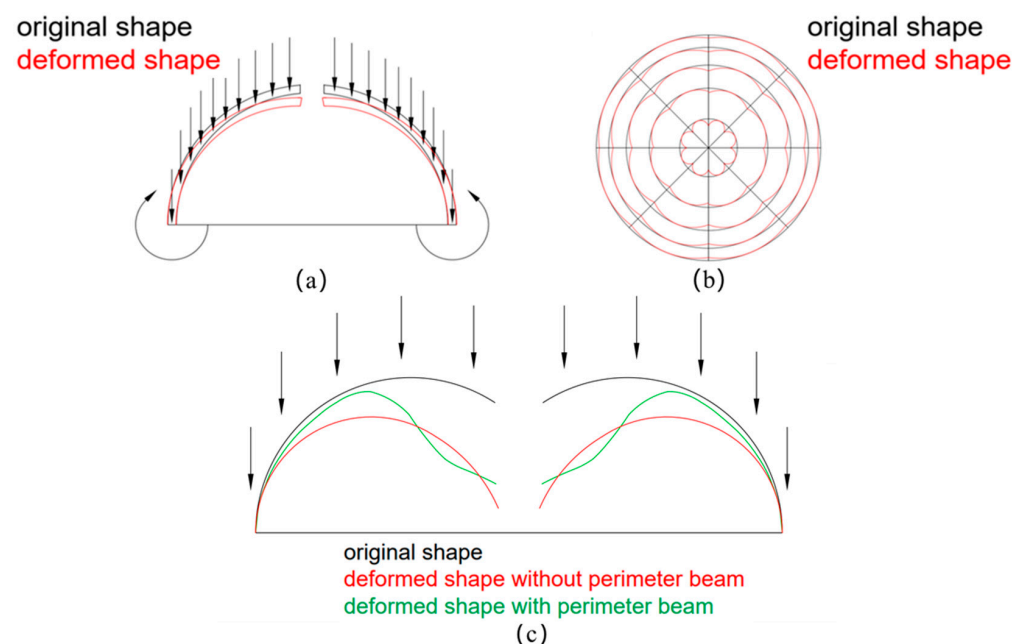


**Figure 6.** The deformation of the structure under vertical loading: (a) load direction demonstration; (b) top view of deformation shape; (c) front view of deformation shape.

When the spindle torus experiences lateral load, the columns in the windward side will experience lateral load. This load will travel along the perimeter beam and cause an overturning moment on the leeward columns, as shown in Figure 7a. The displacement of the leeward and windward wall causes the top perimeter beam to experience tension and lower perimeter beam to experience compression. The expected deformed shapes are shown in Figure 7b,c.

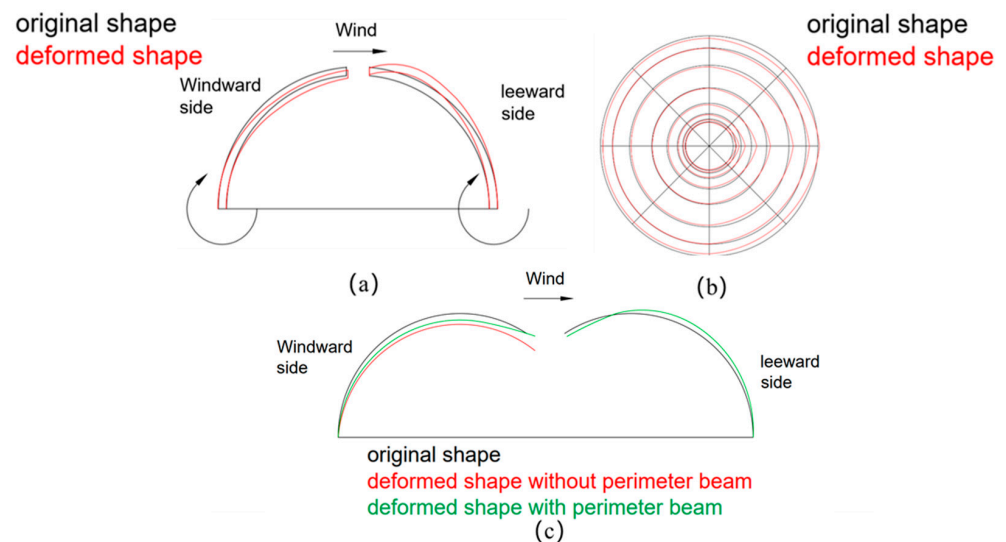


**Figure 7.** The deformation of the structure under lateral loading: (a) load direction demonstration; (b) top view of deformation shape; (c) front view of deformation shape.

#### 4. Numerical Analysis of the Global Behaviors of the Target Structure (Strand7)

##### 4.1. Structural Global Behaviors under Strength Limit State

This section discusses the structural performance of the steel–glass spindle torus structure under strength limit states. The total fiber stress and yield ratio are the main criteria to evaluate the degree of satisfaction of the structure. The linear static solver and nonlinear static solver were used to attain more conservative results. In the nonlinear static solver, the material nonlinearity and geometric nonlinearity were both taken into account. The material was assumed to be isotropic and have the same strength in both tension and compression. The yield stresses of all steel members were assumed to be 350 MPa due to the implementation of grade 350 steel. Due to conservative considerations, it was expected that the steel members in the structure were within the elastic range when subjected to different loads, which implies that displacement caused by the deformation of the steel parts is very small. In Strand7, a zero value of yield ratio indicates that all the steel members are in the elastic state.

Additionally, the structural behaviors of the structure with straight and curved steel members were compared. The intention was to study the extent to which the curved steel members affect the structural performance of the same structure with straight members. To further explore the ultimate capacity of the whole structure, the nonlinear static solver was used to test the maximum load increment when the initial load from the standard was set as a reference load. When Strand7 could not converge, it meant that the finite element program could not generate corresponding displacement values under given load. In other words, this means that this is the critical state of the structure and it cannot withstand more load. Therefore, the corresponding load values can be recorded as the ultimate loads and these values can be compared later. In addition, the global buckling behavior of the whole structure was explored by linear buckling solver, and the first buckling mode with lowest buckling factor was selected as the critical buckling load for the structure.

The ultimate capacity of a structure can be determined by comparing the load factors from nonlinear static and buckling analysis. Out of conservative consideration, the minimum value was selected as the safety factor of the proposed design.

#### 4.1.1. Load Combination: 1.2G + 1.5Q

Table 4 summarizes the total beam fiber stresses of both straight and curved models from both linear and nonlinear analysis under the load combination 1.2G + 1.5Q. Table 5 summarizes the displacements of both straight and curved models from both linear and nonlinear analyses under the load combination 1.2G + 1.5Q.

**Table 4.** Fiber stresses under 1.2G + 1.5Q.

Solver	Straight Member Model		Curved Member Model		Difference
	Maximum Fiber Stress (MPa)	Critical Member	Maximum Fiber Stress (MPa)	Critical Member	
Linear static	130.40	Longitudinal columns on the top ring	132.23	Longitudinal columns on the top ring	1.38%
Nonlinear static	134.82	Longitudinal columns on the top ring	136.06	Longitudinal columns on the top ring	0.96%
Nonlinear static Load increments		2.4	Nonlinear static Load increments	2.2	

**Table 5.** Displacements under 1.2G + 1.5Q.

Solver	Straight Member Model Maximum Displacements (mm)			
	D <sub>x</sub>	D <sub>y</sub>	D <sub>z</sub>	D <sub>xyz</sub>
Linear static	−13.8	−13.0	−299	299
Nonlinear static	−14.1	13.3	−309	230
Solver	Curved Member Model Maximum Displacements (mm)			
	D <sub>x</sub>	D <sub>y</sub>	D <sub>z</sub>	D <sub>xyz</sub>
Linear static	−13.1	13.1	−301	301
Nonlinear static	−13.5	13.5	−312	312

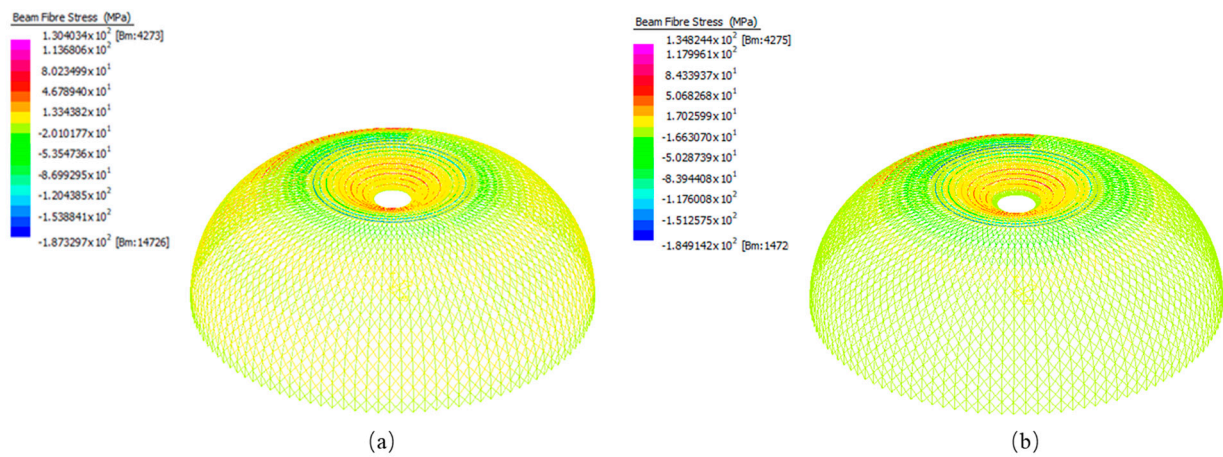
As shown in Table 4 above, the maximum fiber stress (136.1 MPa) was from the nonlinear analysis of the curved structure, and it was smaller than 350 MPa, which indicated that steel members did not yield under the load combination 1.2G + 1.5Q. The longitudinal columns around the top ring experienced maximum fiber stress and little difference between the results from straight member and curved member models.

The total fiber stress distributions of curved and straight member forming both linear and nonlinear analyses are shown in Figures 8 and 9a,b.

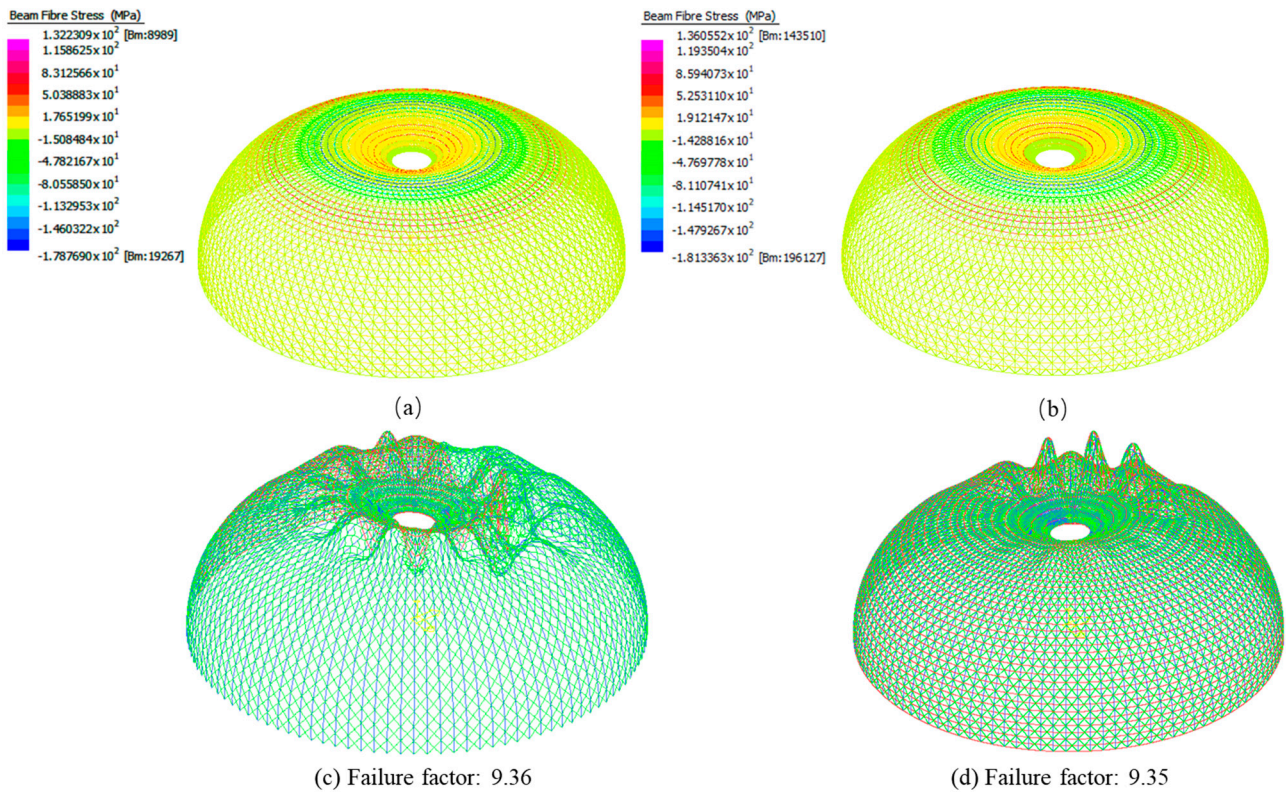
#### 4.1.2. Load Combination: 1.35G

Table 6 summarizes the total beam fiber stresses of both straight and curved models from both linear and nonlinear analysis under the load combination 1.35G. Table 7 summarizes the displacements of both straight and curved models from both linear and nonlinear analysis under the load combination 1.35G.

As shown in Table 6, the maximum fiber stress (103.07 MPa) was from the nonlinear analysis of the curved structure, and it was smaller than 350 MPa, which indicated that the steel members did not yield under the load combination 1.35G. The longitudinal columns around the top ring experienced maximum fiber stress and little difference between the results from straight member and curved member models.



**Figure 8.** (a) Linear analysis of total fiber stress of straight member model under 1.2G + 1.5Q; (b) nonlinear analysis of total fiber stress of straight member model under 1.2G + 1.5Q.



**Figure 9.** (a) Linear analysis of total fiber stress of curved member model under 1.2G + 1.5Q; (b) nonlinear analysis of total fiber stress of curved member model under 1.2G + 1.5Q; (c) linear buckling analysis of the straight member model under 1.2G + 1.5Q; (d) linear buckling analysis of the curved member model under 1.2G + 1.5Q.

Table 6. Fiber stresses under 1.35G.

Solver	Straight Member Model		Curved Member Model		Difference
	Maximum Fiber Stress (MPa)	Critical Member	Maximum Fiber Stress (MPa)	Critical Member	
Linear static	99.02	Longitudinal columns on the top ring	100.38	Longitudinal columns on the top ring	1.37%
Nonlinear static	102.11	Longitudinal columns on the top ring	103.07	Longitudinal columns on the top ring	0.94%
Nonlinear static Load increments		3.1	Nonlinear static Load increments	2.7	

Table 7. Displacements under 1.35G.

Solver	Straight Member Model Maximum Displacements (mm)			
	D <sub>x</sub>	D <sub>y</sub>	D <sub>z</sub>	D <sub>xyz</sub>
Linear static	−10.6	99.1	−227	227
Nonlinear static	−10.8	10.2	−234	234
Solver	Curved Member Model Maximum Displacements (mm)			
	D <sub>x</sub>	D <sub>y</sub>	D <sub>z</sub>	D <sub>xyz</sub>
Linear static	9.99	−9.99	−229	229
Nonlinear static	10.3	10.3	−236	236

The total fiber stress distribution of curved and straight members formed both linear and nonlinear analyses, as shown in Figures 10 and 11a,b.

As shown in Figure 11c,d, with a load combination 1.2G + 1.5Q, the buckling factors for both curved and straight models were almost the same, whereas the curvature of the steel members resulted in a significant difference between buckling shapes under 1.35G. From the nonlinear static analysis and linear buckling analysis, the safety factor in this load combination should be 2.7, and this structure is governed by the yielding of the members instead of buckling.

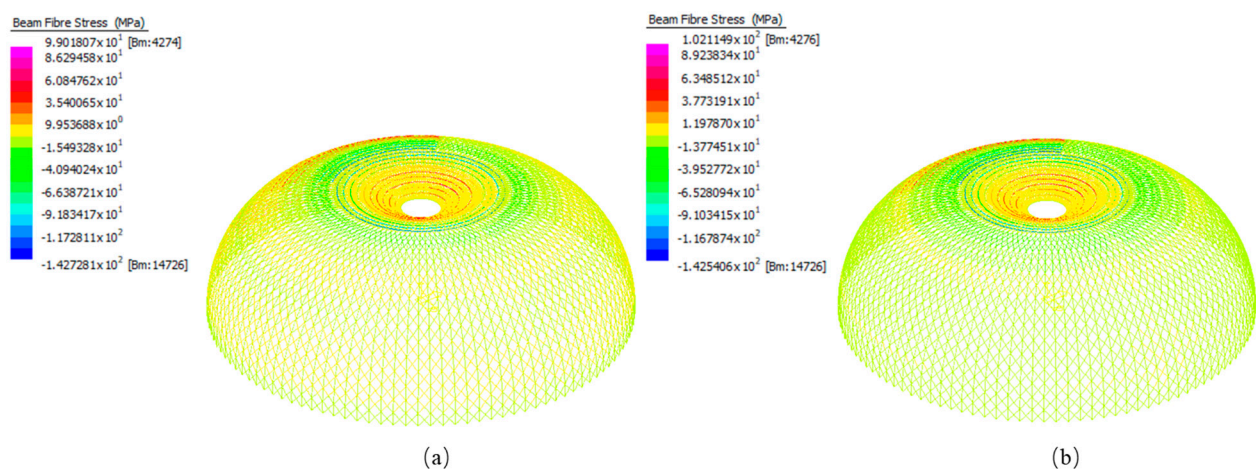
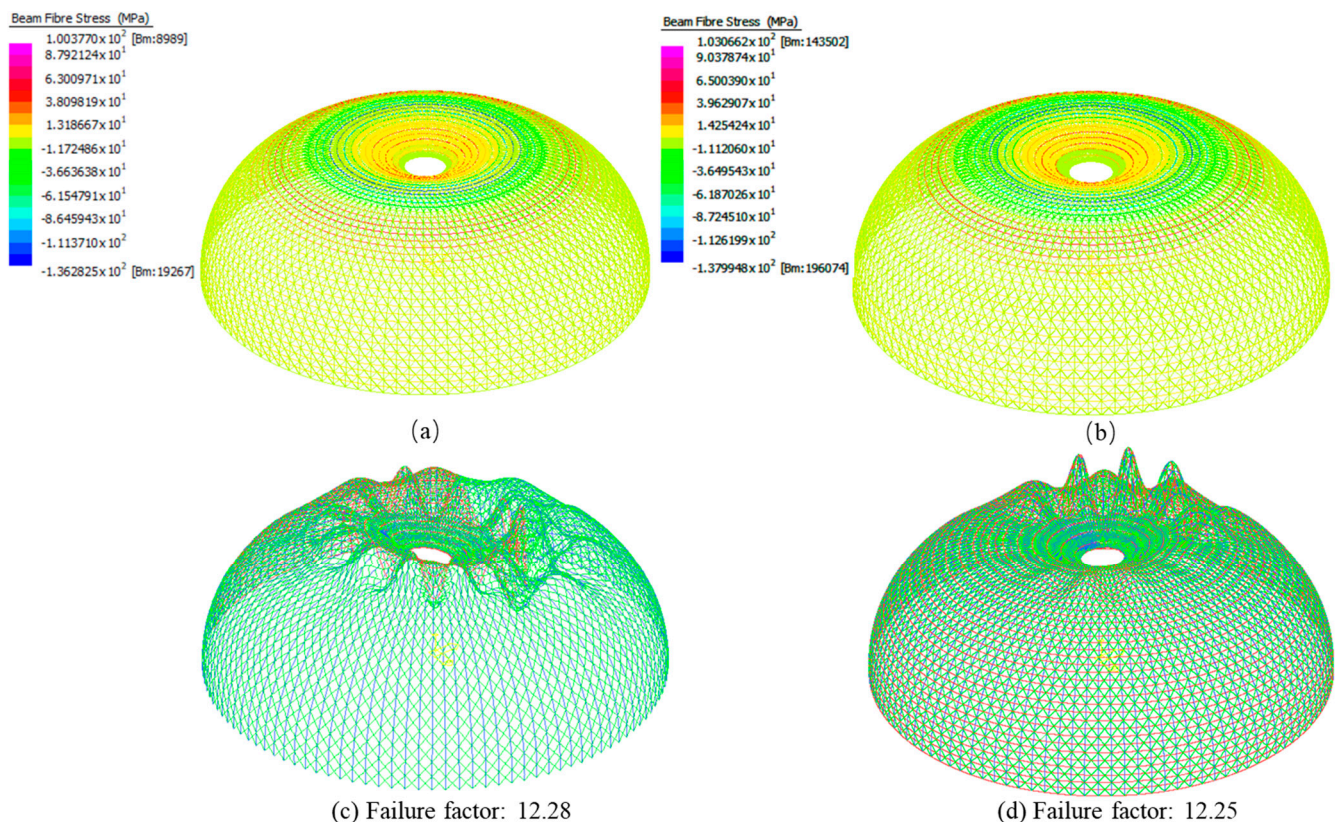


Figure 10. (a) Linear analysis of total fiber stress of straight member model under 1.35G; (b) nonlinear analysis of total fiber stress of straight member model under 1.35G.



**Figure 11.** (a) Linear analysis of total fiber stress of a curved member model under 1.35G; (b) nonlinear analysis of total fiber stress of a curved member model under 1.35G; (c) linear buckling analysis of the straight member model under 1.35G; (d) linear buckling analysis of the curved member model under 1.35G.

#### 4.1.3. Load Combination: 1.2G + W

Table 8 summarizes the total beam fiber stresses of both straight and curved models from both linear and nonlinear analyses under the load combination 1.2G + W. Table 9 summarizes the displacements of straight and curved models from both linear and nonlinear analyses under the load combination 1.2G + W.

As shown in Table 8 above, the maximum fiber stress (204.51 MPa) was from the nonlinear analysis of the curved structure, and it was smaller than 350 MPa, which indicates that the steel members did not yield under the load combination 1.2G + W. Unlike the previous load combinations, it was found that the maximum fiber stress increased significantly (more than 60%) from the straight member model to curved member model under the same loading conditions. In the previous load combinations, the direction of the loads was purely downwards; the wind load acted in the plane of curvature in this case. Additionally, the nonlinear static load increments decreased significantly. Thus, it can be concluded that the loading capacity is sensitive to the curvature of the members when the loads are acting in the plane of curvature.

The total fiber stress distribution of curved and straight members from both linear and nonlinear analyses are shown in Figure 12a,b.

As shown in Figure 13c,d, unlike the previous two load combinations with little difference between buckling factors, the buckling factors for both curved and straight models, in this case, exhibited a significant difference, which was around 42%. This means that the wind load does play an important role in this structural performance, which again proves that the structural performance of the beams is sensitive to the curvature of the beam under the loads in the plane of curvature. From the nonlinear static analysis and linear buckling analysis, the safety factor in this load combination should be 1.6, and this structure is governed by the yielding of the members instead of buckling.

Table 8. Fiber stresses under 1.2G + W.

Solver	Straight Member Model		Curved Member Model		Difference
	Maximum Fiber Stress (MPa)	Critical Member	Maximum Fiber Stress (MPa)	Critical Member	
Linear static	117.27	Longitudinal columns on the top ring	191.56	Longitudinal columns on the top ring	63.34%
Nonlinear static	123.48	Longitudinal columns on the top ring	204.51	Longitudinal columns on the top ring	65.62%
Nonlinear static load increments		3.3	Nonlinear static load increments	1.6	

Table 9. Displacements under 1.2G + W.

Solver	Straight Member Model Maximum Displacements (mm)			
	D <sub>x</sub>	D <sub>y</sub>	D <sub>z</sub>	D <sub>xyz</sub>
Linear static	23.7	−17.9	−227	227
Nonlinear static	22.6	−16.8	−230	230
Solver	Curved Member Model Maximum Displacements (mm)			
	D <sub>x</sub>	D <sub>y</sub>	D <sub>z</sub>	D <sub>xyz</sub>
Linear static	31.5	21.8	−420	420
Nonlinear static	31.5	21.9	−398	398

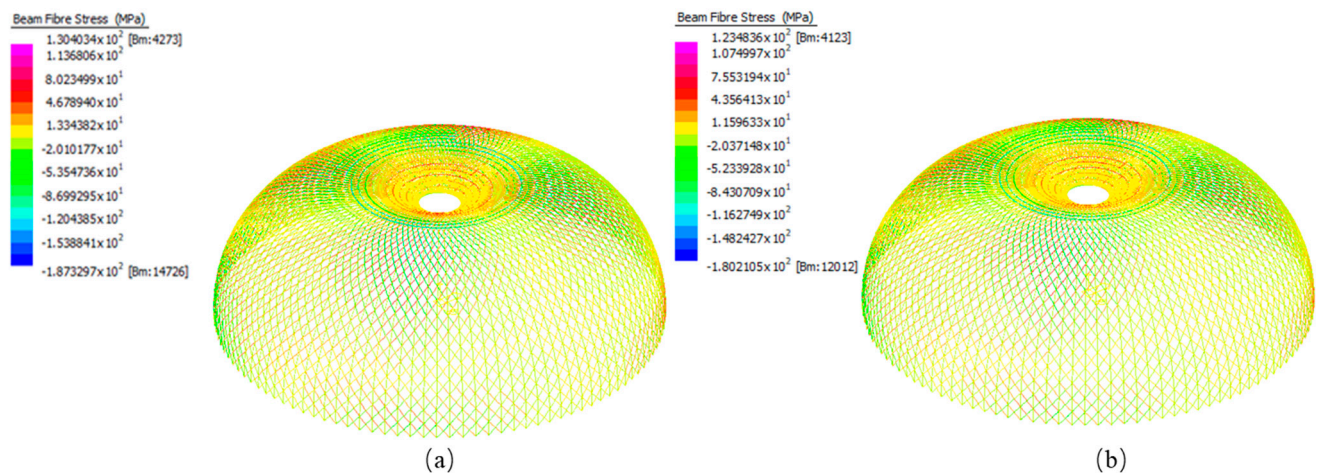
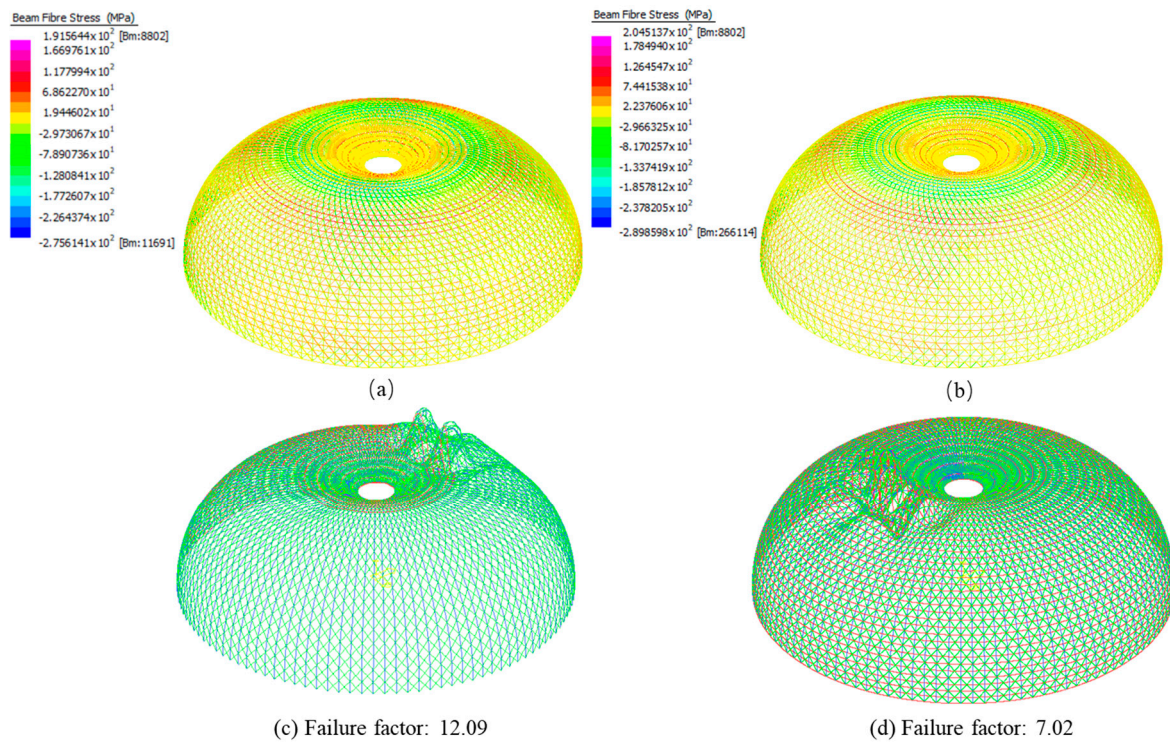


Figure 12. (a) Linear analysis of total fiber stress of straight member model under 1.2G + W; (b) nonlinear analysis of total fiber stress of straight member model under 1.2G + W.

Through the strength limit state analysis, the designed steel–glass structure performed well under the proposed load combinations according to AS1170 [31]. All the steel members were in the elastic state. Thus, the yield ratio was 0 everywhere. All structural steel members were within the elastic range; therefore, all deformations were quite small and there were no plastic deformations, which indicates that the capacity of the structure was not reached. Therefore, the proposed structure is safe under the proposed load combinations. According to the results from the load combinations 1.2G + 1.5Q and 1.35G, the loads are all acting downwards, as shown in Figure 14a,b. At this time, the curvature of the beams will not cause much difference regarding the mechanical performances comprising the maximum fiber stress and critical buckling load. However, the results of the

load combination 1.2G + W indicate that the curvature of the beams will cause significant differences (almost 60% for maximum fiber stress and almost 40% for buckling load) when there are loads acting in the plane of curvature, such as in Figure 14c,d. Additionally, the capacity of the beams tended to be reduced due to curvature. Hence, it is also necessary to explore how the curvature will influence the load-bearing capacity under the load in the plane of curvature.



**Figure 13.** (a) Linear analysis of total fiber stress of curved member model under 1.2G + W; (b) non-linear analysis of total fiber stress of curved member model under 1.2G + W; (c) linear buckling analysis of the straight member model under 1.2G + W; (d) linear buckling analysis of the curved member model under 1.2G + W.

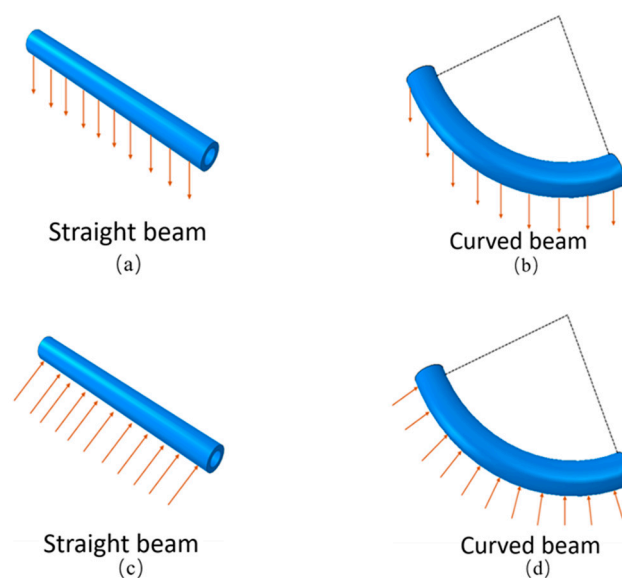


**Figure 14.** Demonstration of different loading directions for straight and curved beams: (a) the gravity load for a straight beam; (b) the gravity load for a curved beam; (c) the wind load for a straight beam; (d) the wind load for a curved beam.

#### 4.2. Structural Global Behaviors under Serviceability Limit State

The global behaviors of both straight member and curved member models were tested in Strand7, and the results are presented in this section. The developed models were analyzed using the linear static solver and the non-linear static solver. According to AS1170 [31], the following two load combinations should be considered for the designed spindle torus:

- Load combination 1:  $G + 0.7Q$ ;
- Load combination 2:  $G + 0.7Q + W$ .

##### 4.2.1. Maximum Structural Displacement of the Designed Structure under Linear Static Analysis

For the sake of simplifying the model, it was assumed that the glass on the surface of the structure was smooth enough so that the effects of wind friction on the surface were minimal and therefore could be disregarded. When calculating the wind load ( $W$ ) on the structure, only the wind perpendicular to the spindle torus surface was considered effective. With the estimated dead load, live load and wind load, the structural performance of the designed spindle torus was simulated in Strand 7. At the initial stage, the linear static solver was used. From the linear static analysis, the maximum structural displacement in each load combination is tabulated in Table 10.

**Table 10.** Maximum structural displacement under serviceability limit state (linear static analysis).

The Straight Member Model					
Load Combination	$D_x$ (mm)	$D_y$ (mm)	$D_z$ (mm)	$D_{xy}$ (mm)	$D_{xyz}$ (mm)
$G + 0.7Q$	−9.89	9.30	−213.63	9.90	213.64
$G + 0.7Q + W$	24.19	−18.20	−238.23	24.19	238.60
The Curved Member Model					
Load Combination	$D_x$ (mm)	$D_y$ (mm)	$D_z$ (mm)	$D_{xy}$ (mm)	$D_{xyz}$ (mm)
$G + 0.7Q$	−9.373	9.373	−215.28	9.373	215.29
$G + 0.7Q + W$	32.00	22.09	−409.44	32.00	409.72

According to the numerical analysis results of two constructed models, under both load combinations, the structural displacement along the  $z$ -axis was significantly higher than the structural displacement along the  $x$ - and  $y$ -axes. Therefore, under the serviceability limit state, the structural displacement was governed by gravity loads. This is mainly due to the excessive use of structural components. In the proposed design, 120 longitudinal columns were configured with an angular spacing of  $3^\circ$ . Between the longitudinal columns, 9840 cross-bracings were used. The designed structure contained 42 perimeter beams, and each perimeter beam could be further subdivided into 120 beam segments. At a high level, the length of the perimeter beam segment was relatively small. For instance, at the bottom of the central opening, the length of the perimeter beam segment was only 0.102 m. All these design redundancies resulted in the over-reinforced structure, making the gravity load more critical than the applied wind load. Under serviceability limit state, the load combination  $G + 0.7Q + W$  in the curved member model always exhibited the maximum beam displacement. For structural displacement along three axes, the maximum beam displacement along the  $x$ -axis was observed at the top of the windward surface. The maximum structural displacements along the  $y$ -axis and  $z$ -axis were both observed at the central opening of the spindle torus. The maximum total displacement ( $D_{xyz}$ ) of the designed structure was also observed at the central opening.

According to AS1170.0 [36], Table C1, the maximum lateral deflection of roof-supporting elements should be smaller than span/400. Given the radius for each longitudinal column being  $125^\circ$ , the length of each longitudinal column could be calculated in Equation (1):

$$L_{lc} = \frac{125}{360} \times 2\pi \times 25 = 54.54 \text{ m} \quad (1)$$

For a longitudinal column spanning 54.54 m, the maximum allowable displacement was demonstrated in Equation (2):

$$v_{\max} = \frac{54.54}{400} = 136.4 \text{ mm} \quad (2)$$

Under serviceability limit state, the maximum lateral deflection  $D_{xy,\max}$  was observed in the curved member model under load combination  $G + 0.7Q + W$ , which was equal to 32 mm. The maximum lateral displacement was significantly smaller than the maximum allowable displacement in AS1170 [31]; therefore, the structural design was feasible.

The total displacement ( $D_{xyz}$ ) under the load combination  $G + 0.7Q$  was analyzed using a linear static solver. The total beam displacement  $D_{xyz}$  in two numerical models is demonstrated in Figure 15a,b.

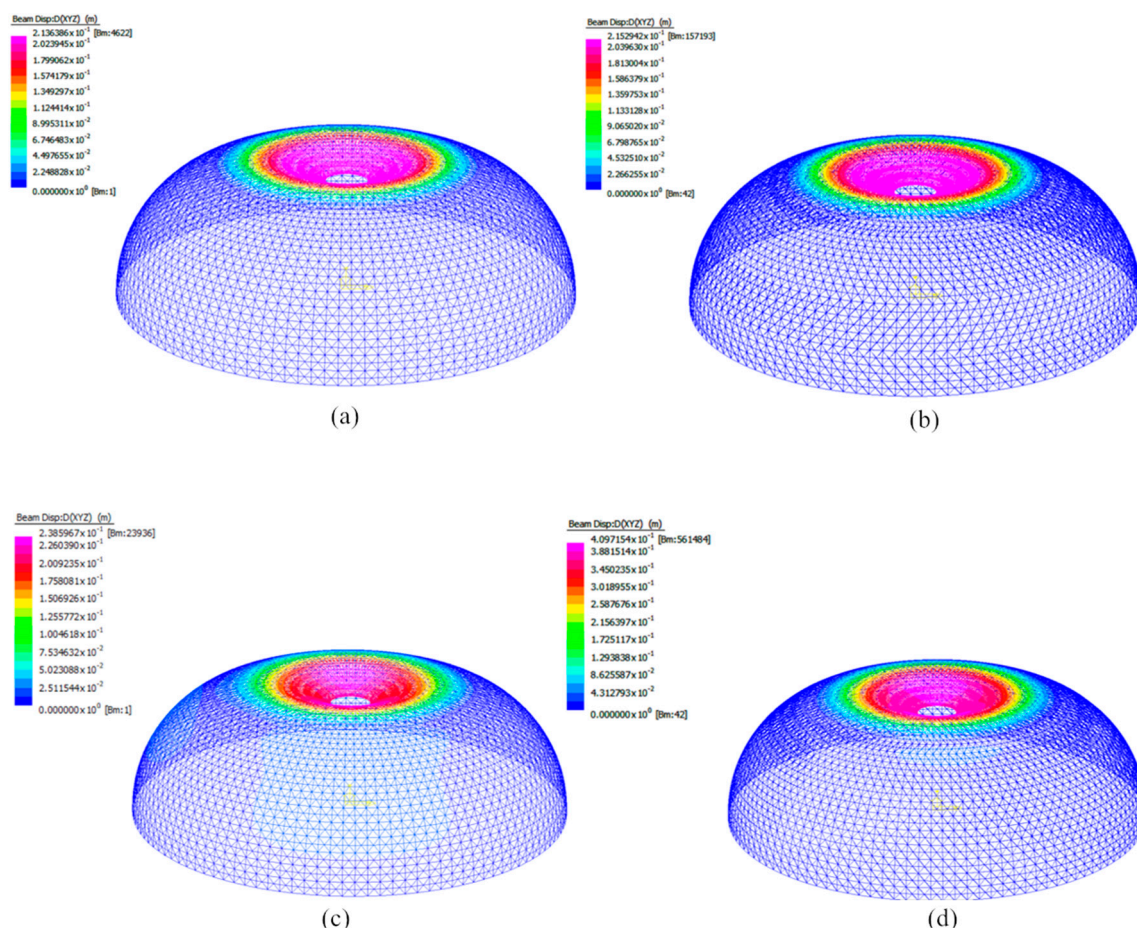


**Figure 15.** (a) Total beam displacement in the straight member model by linear static analysis ( $G + 0.7Q$ ); (b) total beam displacement in the curved member model by linear static analysis ( $G + 0.7Q$ ); (c) total beam displacement in the straight member model by linear static analysis ( $G + 0.7Q + W$ ); (d) total beam displacement in the curved member model by linear static analysis ( $G + 0.7Q + W$ ).

As indicated in Figure 15a,b, under load combination  $G + 0.7Q$ , the maximum total displacement in two numerical models was 213.64 mm and 215.29 mm, respectively. The

second numerical model using curved beam elements exhibited higher structural displacement than the first model. This could be attributed to the longer span of the curved beam elements, which resulted in a higher gravity load. However, because the difference between the total deflection in two numerical models was negligible, the global behavior of two designed structures under load combination  $G + 0.7Q$  was almost identical.

The total displacement ( $D_{xyz}$ ) under the load combination  $G + 0.7Q + W$  was analyzed through the linear static solver. The total beam displacement  $D_{xyz}$  in two numerical models is demonstrated in Figure 15c,d.

As indicated by Figure 15c,d under the load combination  $G + 0.7Q + W$ , the maximum total displacement in the two numerical models was 238.60 mm and 409.72 mm, respectively. The second numerical model using curved beam elements exhibited a much higher structural displacement than the first model. The large total displacement in the curved member model can be explained by the loading direction of the wind load. As concluded in Section 5, the dead load and live load in both load combinations were always configured in the vertical direction, which did not exert significantly different structural impacts on the straight and curved beam elements. However, the wind load was always applied in the direction perpendicular to the structural surface. For curved beam elements, the applied wind load was concentrated at a certain point, which resulted in excessive beam deflection. The excessive total displacement in the curved member model could also be attributed to the longer span and intensive subdivision of the curved beam element. In the model, the curved beam element was not perfectly curved. Each curved beam element consisted of multiple straight beam elements. Therefore, intensive subdivisions were made for the curved beam. However, in the straight member model, no further subdivision was made for the straight beam element. Therefore, the beam displacement in a straight member model could only be observed from the displacement at two end nodes, resulting in inaccurate structural displacement. The excessive total displacement in the curved member model required further attention, because it increased the risk of structural failure.

#### 4.2.2. Maximum Structural Displacement of the Designed Structure under Nonlinear Static Analysis

After analyzing the global behavior of the designed spindle torus using the linear static solver, the nonlinear static solver was then used to analyze the structural performance. In this case, the same load combinations in the serviceability limit state were used. With the start loading factor being 0 and the end loading factor being 1, ten load steps were configured in this nonlinear static analysis. The loading factor was gradually increased with an increment of 0.1. From the nonlinear static analysis, the maximum structural displacement values in each load combination are tabulated in Table 11.

**Table 11.** Maximum structural displacement under serviceability limit state (non-linear static analysis).

The Straight Member Model Using Straight Beam Elements					
Load Combination	$D_x$ (mm)	$D_y$ (mm)	$D_z$ (mm)	$D_{xy}$ (mm)	$D_{xyz}$ (mm)
$G + 0.7Q$	−10.01	9.44	217.83	10.02	217.84
$G + 0.7Q + W$	23.07	−17.15	−240.50	23.07	240.79
The Curved Member Model Using Curved Beam Elements					
Load Combination	$D_x$ (mm)	$D_y$ (mm)	$D_z$ (mm)	$D_{xy}$ (mm)	$D_{xyz}$ (mm)
$G + 0.7Q$	9.56	9.56	219.64	9.56	219.65
$G + 0.7Q + W$	32.01	22.23	−432.84	32.02	432.06

According to the numerical analysis results of two constructed models, under both load combinations, the structural displacement along the  $z$ -axis was significantly higher than the structural displacement along the  $x$ - and  $y$ -axis. Hence, under the serviceability limit state, the structural displacement was always governed by gravitational load. This was mainly due to the excessive use of structural components. Compared with the maximum

displacement in the linear static analysis, the maximum structural displacement obtained from the non-linear static analysis was slightly higher. The non-linear solver considers both geometrical and material non-linearity; therefore, under non-linear static analysis, load combination  $G + 0.7Q + W$  in the curved member model always exhibited the maximum beam displacement. For structural displacement along three axes, the maximum beam displacement along the  $x$ -axis was observed at the top of the windward surface. The maximum structural displacements along the  $y$ -axis and  $z$ -axis were both observed at the central opening of the spindle torus. The maximum total displacement ( $D_{xyz}$ ) of the designed structure was also observed at the central opening.

According to AS1170 [36], Table C1, the maximum lateral deflection of roof supporting elements should be smaller than  $\text{span}/400$ . Given the radian for each longitudinal column being  $125^\circ$ , the length of each longitudinal column can be calculated by Equation (3):

$$L_{lc} = \frac{125}{360} \times 2\pi \times 25 = 54.54 \text{ m} \quad (3)$$

For a longitudinal column spanning 54.54 m, the maximum allowable displacement was demonstrated in Equation (4):

$$v_{\max} = \frac{54.54}{400} = 136.4 \text{ mm} \quad (4)$$

Under the serviceability limit state, the maximum lateral deflection  $D_{xy,\max}$  was observed in load combination  $G + 0.7Q + W$ , the curved member model, which was equal to 32.02 mm. The maximum lateral displacement was significantly smaller than the maximum allowable displacement in AS1170 [36]; therefore, the structural design was feasible.

The total displacement  $D_{xyz}$  under the load combination  $G + 0.7Q$  was analyzed under the nonlinear static solver. As indicated by Figure 16a,b, under load combination  $G + 0.7Q$ , the maximum total displacement in two numerical models was 217.88 mm and 219.65 mm, respectively. Compared with the first model using straight beam elements, the second numerical model using curved beam elements exhibited higher structural displacement. This can be attributed to the longer span of the curved beam elements, which led to a higher gravitational load. Compared with the analysis results from linear static analysis, the results from the non-linear static analysis were slightly higher. The non-linear static analysis of the designed structure demonstrated a more realistic structural response under the proposed load, because geometrical and material non-linearity were considered in this solver.

The total displacement  $D_{xyz}$  under the load combination  $G + 0.7Q + W$  was analyzed under the nonlinear static solver. The total beam displacement  $D_{xyz}$  in two numerical models is demonstrated in Figure 16c,d:

As indicated by Figure 16c,d above, under load combination  $G + 0.7Q + W$ , the maximum total displacement in two numerical models was 240.79 mm and 432.06 mm, respectively. The second numerical model using curved beam elements exhibited much more significant structural displacement than the first model. This complied with the results of the linear static analysis. As explained in the previous section, the large difference may be ascribed to the loading direction of the wind load and the longer span/intensive subdivision of curved beam elements. Similar to load combination  $G + 0.7Q$ , load combination  $G + 0.7Q + W$  under non-linear static analysis also exhibited higher structural displacement than load combination  $G + 0.7Q + W$  under linear static analysis, because geometrical and material non-linearities were both considered in the non-linear solver.

Thus, under both linear and non-linear static analysis of the serviceability limit state, the maximum lateral displacement of the designed structure satisfied the design limitation in AS1170.0 [36]. Therefore, the designed structure is technically feasible. For the numerical model using curved beam elements, the total displacement in load combination  $G + 0.7Q + W$  was significantly more remarkable than the total displacement obtained in the numerical model using straight beam elements. This excessive total displacement could be attributed

to the loading direction of the wind load, the longer beam length of the curved beam, and the intensive subdivision of the curved structural components. Under non-linear static analysis, all structural components tended to exhibit higher displacement, because geometrical and material non-linearity were both considered in the solver.

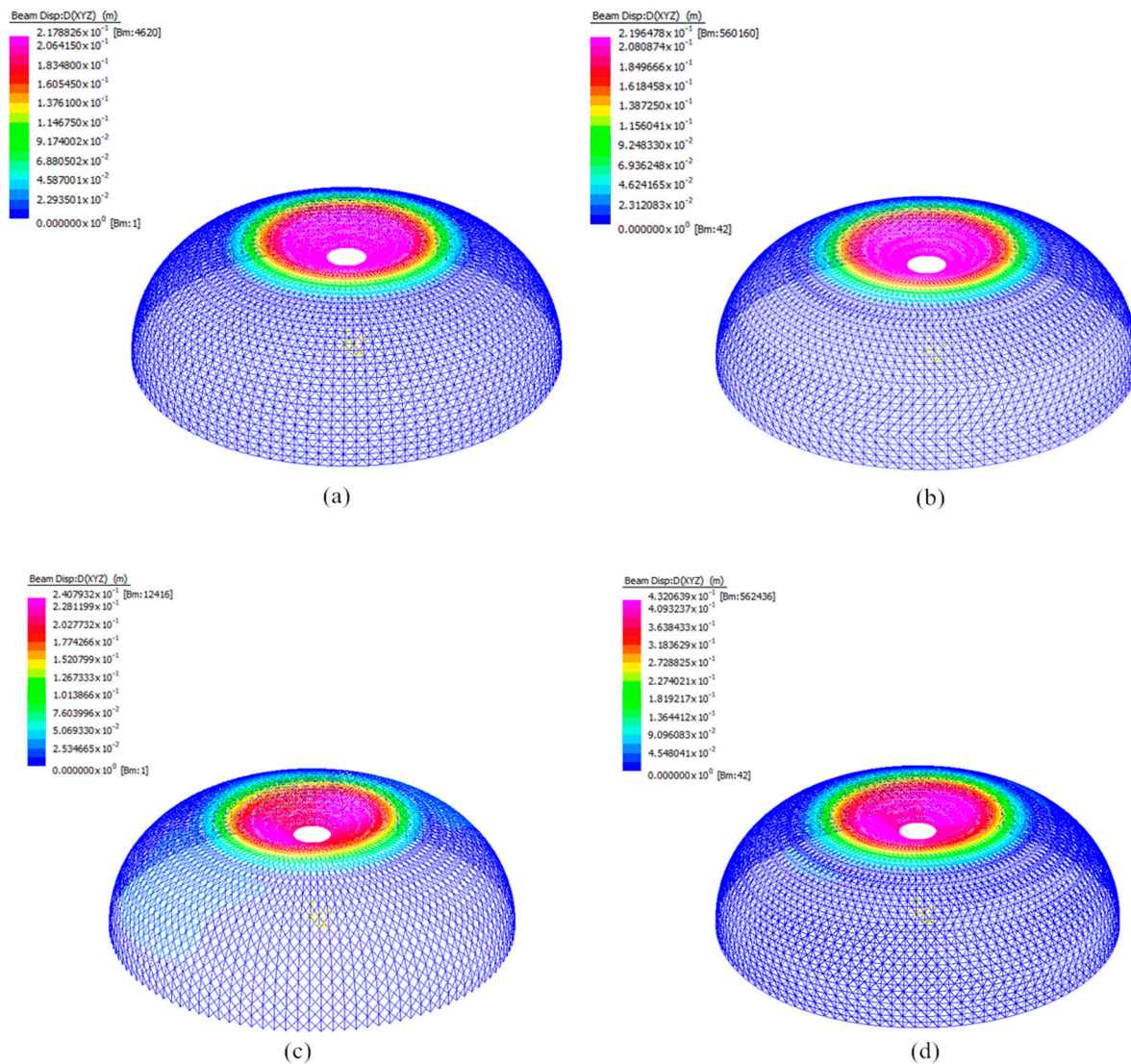


**Figure 16.** (a) Total beam displacement in the straight member model by nonlinear static analysis ( $G + 0.7Q$ ); (b) total beam displacement in the curved member model by nonlinear static analysis ( $G + 0.7Q$ ); (c) total beam displacement in the straight member model by nonlinear static analysis ( $G + 0.7Q + W$ ); (d) total beam displacement in the curved member model by nonlinear static analysis ( $G + 0.7Q + W$ ).

#### 4.2.3. Maximum Axial Stress in All Structural Components under Serviceability Limit State

Both linear static analysis and non-linear static analysis were conducted in two numerical models, and the results are presented in this section. For each model, two serviceability load combinations were considered. According to the numerical analysis results, the maximum axial stress on each type of structural component is tabulated in Table 12.

**Table 12.** Maximum axial stress on each type of structural component (Non-linear static analysis).

The Straight Member Model Using Straight Beam Elements		
Load Combination	Solver	Axial Stress (MPa)
G + 0.7Q	Linear static	52.75
G + 0.7Q	Non-linear static	53.14
G + 0.7Q + W	Linear static	81.03
G + 0.7Q + W	Non-linear static	77.76
The Curved Member Model Using Curved Beam Elements		
Load Combination	Solver	Axial Stress (MPa)
G + 0.7Q	Linear static	51.62
G + 0.7Q	Non-linear static	51.89
G + 0.7Q + W	Linear static	103.04
G + 0.7Q + W	Non-linear static	107.57

According to the maximum axial stress in Table 12, under serviceability limit state, the maximum axial stress in all structural components was 107.57 MPa. The yield stress of all selected sections was equal to 350 MPa; therefore, the designed structure will not experience plastic deformation under the serviceability limit state. In the straight member model, due to the addition of non-symmetric wind load, the maximum axial stress in load combination G + 0.7Q + W was 50% higher than the maximum load combination in load combination G + 0.7Q. However, in the curved member model, the maximum axial stress induced by load combination G + 0.7Q + W was almost 100% higher than the maximum axial stress in load combination G + 0.7Q. The analysis result of axial stress complied with the structural displacement results in previous sections, indicating that the beam curvature will result in a great difference in mechanical behaviors when considering the wind load. In addition, this difference may also be attributed to the longer span of the curved beam and the intensive subdivision of curved structural components.

## 5. Numerical Analysis of the Local Member Behaviors of Target Structures (Strand7 and ABAQUS)

### 5.1. The Investigation of the Effective Length Factor of the Longitudinal Column

After investigating the global structural behavior under different load combinations, the local member behavior of the longitudinal column was also investigated to optimize the design of the longitudinal column. In the designed structure, the longitudinal column mainly sustained axial load. Hence, the buckling behavior of the longitudinal column under axial load was investigated. Based on different boundary conditions, the connection of the longitudinal columns could be divided into two major groups, which included the braced column connection and the sway column connection. Using numerical analysis, the buckling loads of six braced and sway column cases were determined. The effective length factor of each column case was determined according to the obtained buckling load. A smaller effective length factor  $k$  indicates a more stable structure.

#### 5.1.1. The Effective Length Factor for Braced Longitudinal Columns

The longitudinal column was mainly subjected to axial compressive load in the designed structure. Under axial load, the effective length factor of columns in frames relied on the ratio between the compression member stiffness and the end restraint stiffness [38]. Based on different boundary conditions, the effective length factor of the braced members under compressive load varied from 0.5 to 1 [39]. In AS4100 [8], the effective length of a straight member under compressive load is defined. However, the feasibility of AS4100 [8] for the designed structure still needed to be explored because of the curved steel column sections used in this design. The non-dimensional term  $L/R$  ratio was used to determine the initial bentness of the designed column rather than the curvature. The term  $L$  refers to the chord length, and  $R$  refers to the radius. This section will discuss the feasibility of the

AS4100 [8] effective length factor regarding the braced curved column. The critical elastic buckling loads were determined by the linear buckling solver in Strand7, and the results are listed in Table 13. The obtained results complied with the numerical analysis conducted by [40]. With the increase in L/R ratio, the buckling load of the curved column under axial compression experienced a significant decrease.

**Table 13.** The elastic buckling loads for braced longitudinal columns.

L/R Ratio	Elastic Buckling Load (kN)		
	Brace Member Case 1	Brace Member Case 2	Brace Member Case 3
0	5858.9	3117.89	1567.75
0.2	5849.19	3111.3	1566.79
0.4	5819.14	3090.88	1563.87
0.6	5774.62	3058.29	1558.75
0.8	5703.19	3009.69	1550.89
1	5614.58	2945.51	1540.46
1.2	5503.91	2862.52	1525.82
1.4	5367.27	2755.41	1505.51
1.6	5195.23	2612.96	1476.03
1.8	4960.11	2404.55	1428.02
2	4337.6	2277.4	1256.86

The three braced member cases in Figure 17 refer to the braced column with three different boundary conditions. As indicated by AS4100 [8], the effective length factors of these braced case are 0.7, 0.85 and 1, respectively. To effectively determine the feasibility of calculating the compressive capacity of curved members using AS4100 [8], the actual effective length factor for each braced column case needs to be determined and compared with the given value in AS4100 [8].

	Braced member			Sway member		
Buckled shape						
Effective length factor ( $k_e$ )	0.7	0.85	1.0	1.2	2.2	2.2
Symbols for end restraint conditions	= Rotation fixed, translation fixed	= Rotation fixed, translation free	= Rotation free, translation fixed	= Rotation free, translation free	= Rotation free, translation free	= Rotation free, translation free

**Figure 17.** The effective length factor provided by AS4100.

In this research, the value of  $k$  was derived from the equation of Euler Buckling load. As indicated by AS4100 [8], the Euler buckling load ( $P_e$ ) of a perfectly straight beam can be calculated by Equation (5).

$$P_e = \frac{\pi^2 EI}{(k_e L_0)^2} \quad (5)$$

where  $L_0$  represents the original length of beams,  $E$  is the elastic modulus,  $I$  is the second moment of area, and  $k_e$  represents the effective length factor of beams. In this equation, the critical buckling load of different curved beams can be determined by the linear

buckling solver in Strand7. With the critical buckling load from the numerical analysis, the effective length factor  $k_e$  of different curved beams can then be back-calculated using the Equation (6):

$$k_e = \sqrt{\frac{\pi^2 EI}{P_e L_0^2}} \quad (6)$$

The variation of effective length factor with the change of L/R ratio was investigated and is presented in the following section. In Figure 18, the effective length factor for curved columns with different L/R ratios is demonstrated. All these factors are calculated based on the obtained elastic buckling load and the column chord length.

As shown in Figure 18, with the increase in L/R ratios, the effective length factors of three braced column cases will all increase. The braced member cases 1–3 are fixed–fixed, fixed–pinned and pinned–pinned boundary conditions, respectively. This indicates a decrease in the buckling load capacity of beams. For a curved column, the maximum reasonable L/R ratio is two, because it already represents a half-circle. The effective length factor adopted in AS4100 [8] is greater than the theoretical value due to the consideration of other imperfections. For the braced member case 1 and case 2, the effective length factor was basically safe for curved members because all the numerical effective length factors were lower than the factor specified in AS4100 [8]. However, for braced member case 3, the standard value was unsafe, because the effective length factors from numerical analysis were mostly higher than the value given in AS4100 [8]. To improve the structural stability, a new effective length factor of 1.2 was suggested rather than the standard value in AS4100 [8]. In Figure 19a–c, the critical buckling shapes of each braced case with L/R ratios of 0.4, 1 and 1.8 are demonstrated.

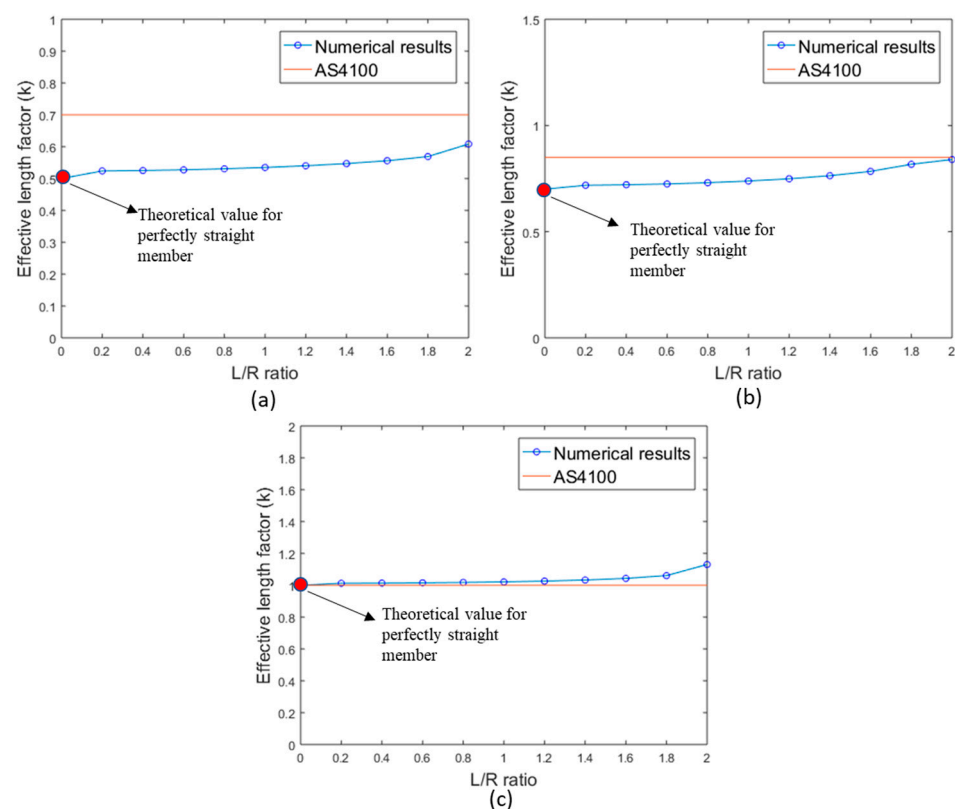


**Figure 18.** The effective length factor ( $k_e$ ) of curved columns under different L/R ratios: (a) braced member case 1; (b) braced member case 2; (c) braced member case 3.

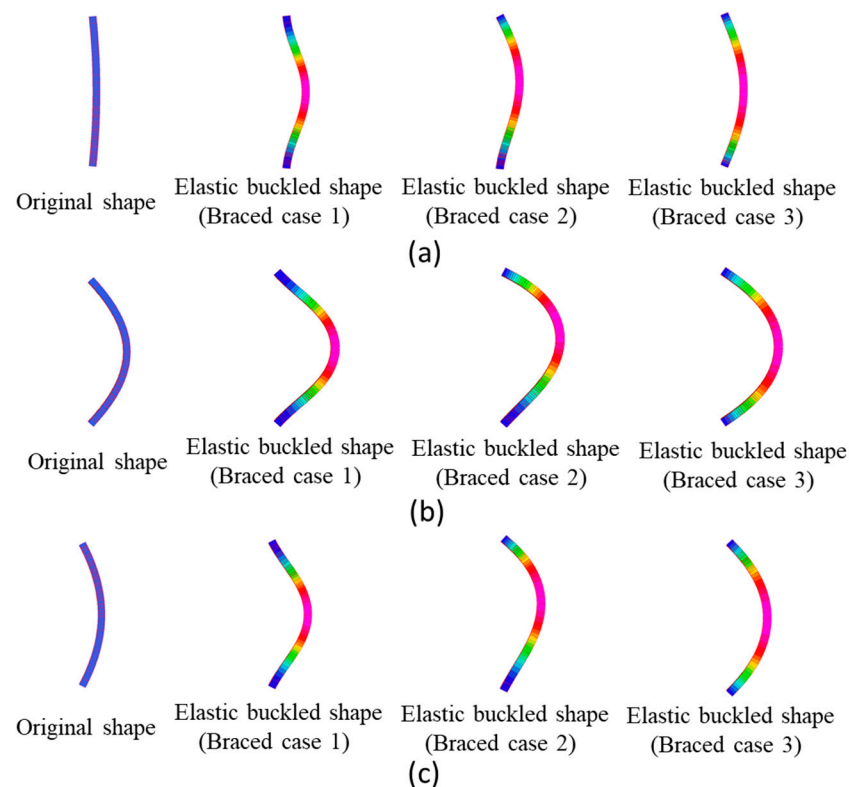


**Figure 19.** (a) The critical elastic buckled shape for the curved column with L/R ratio 0.4; (b) the critical elastic buckled shape for the curved column with L/R ratio 1.0; (c) the critical elastic buckled shape for the curved column with L/R ratio 1.8.

### 5.1.2. The Effective Length Factor for Sway Curved Columns

This section discusses the feasibility of calculating the buckling load of curved sway members using the effective length factor in AS4100 [8]. According to [39], the effective length factor  $k$  for sway members under compressive load can vary from 1 to infinity. To determine the actual effective length factor of curved sway members with different L/R ratios, numerical analysis similar to [41] was conducted. In this case, all numerical models of curved sway members were analyzed in Strand7 using the linear buckling solver. The critical elastic buckling loads of the 11 tested members are listed in Table 14.

**Table 14.** The elastic buckling loads for sway columns.

L/R Ratio	Elastic Buckling Load (kN)		
	Braced Member Case 1	Braced Member Case 2	Braced Member Case 3
0	1567.75	399.037	399.037
0.2	1563.7	398.379	398.379
0.4	1551.27	396.334	396.334
0.6	1531.18	393.03	393.03
0.8	1502.38	388.21	388.21
1	1464.89	381.78	381.78
1.2	1417.87	373.47	373.47
1.4	1359.65	362.79	362.79
1.6	1286.45	348.722	348.722
1.8	1187.63	328.522	328.522
2	945.235	272.492	272.492

Similarly, the diagrams of effective length factor versus L/R ratio under three sway conditions were demonstrated.

As shown in Figure 20a, for sway member case 1, starting from one for a perfectly straight member, the effective length factor  $k$  for a column under sway condition 1 increased with the increase in the L/R ratio. When the L/R ratio of the tested specimen reached 1.83, the effective length factor of the column was equal to the theoretical value of  $k$  in AS4100 [8]. When the L/R ratio of the tested column specimen grew above 1.83, the effective length factor of the column was then beyond the theoretical value of  $k$  in AS4100 [8]. Therefore, for the curved column under sway condition 1, the value of  $k$  in AS4100 [8] could only act as a conservative design factor for curved columns when the L/R ratio of columns was below 1.83. For columns with excessive curvature, the effective length factor  $k$  in AS4100 [8] can no longer be used. To propose some safety margin for the existing design, it was recommended to use 1.5 as the new effective length factor for sway case 1.

As shown in Figure 20b,c, the tested column specimen for sway member cases 2 and 3 shared the same effective length factor under the same L/R ratio. Starting from two for a perfectly straight member, the effective length factor  $k$  for a column under sway condition 2 increased with the increase in the L/R ratio. When the L/R ratio of the tested specimen reached 1.80, the effective length factor of the column was equal to the theoretical value of  $k$  in AS4100 [8]. When the L/R ratio of the tested column specimen grew above 1.80, the effective length factor of the column was then beyond the theoretical value of  $k$  in AS4100 [8]. Therefore, for a curved column under sway condition 2, the value of  $k$  in AS4100 [8] could only act as a conservative design factor for the column when the column's L/R ratio was below 1.80. For columns with excessive curvature, the effective length factor  $k$  in AS4100 [8] can no longer be used. To ensure the structural stability of all curved members under sway cases 2 and 3, it was recommended to use 2.5 as the new effective length factor for both sway cases. In Figure 21a–c, the critical buckling shapes of each sway case with L/R ratios of 0.4, 1 and 1.8 are demonstrated.

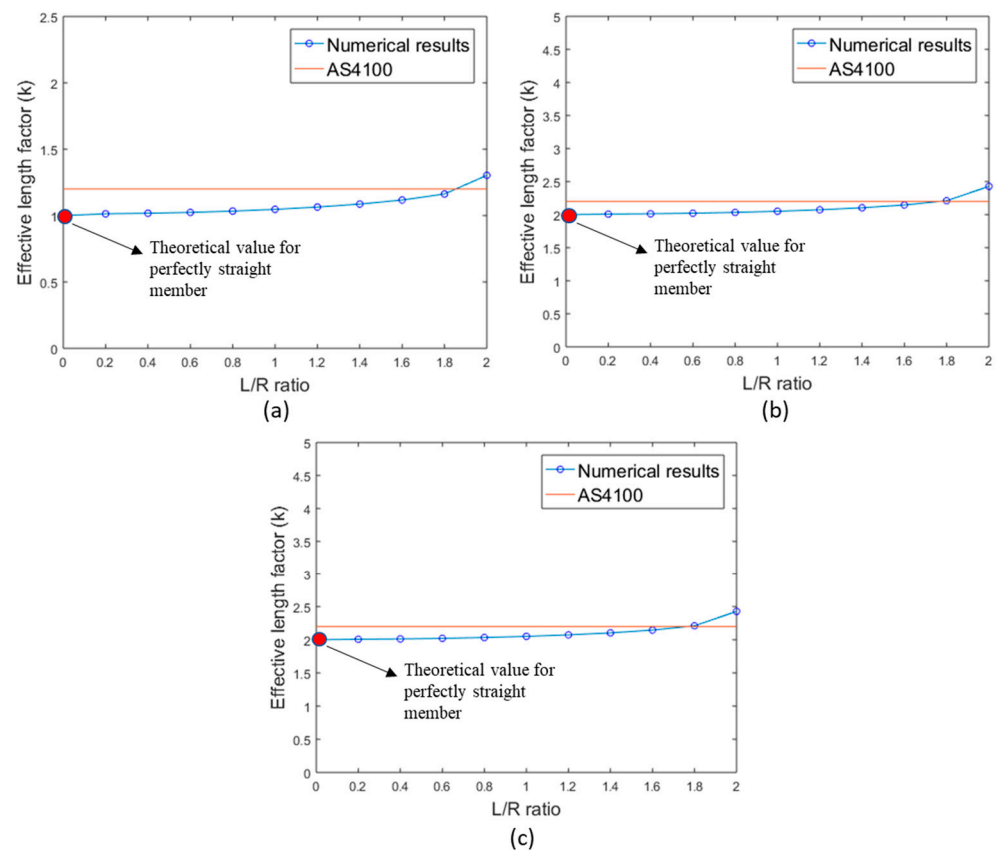


**Figure 20.** The effective length factor ( $k_e$ ) of curved beams under different L/R ratios: (a) sway member case 1; (b) sway member case 2; (c) sway member case 3.

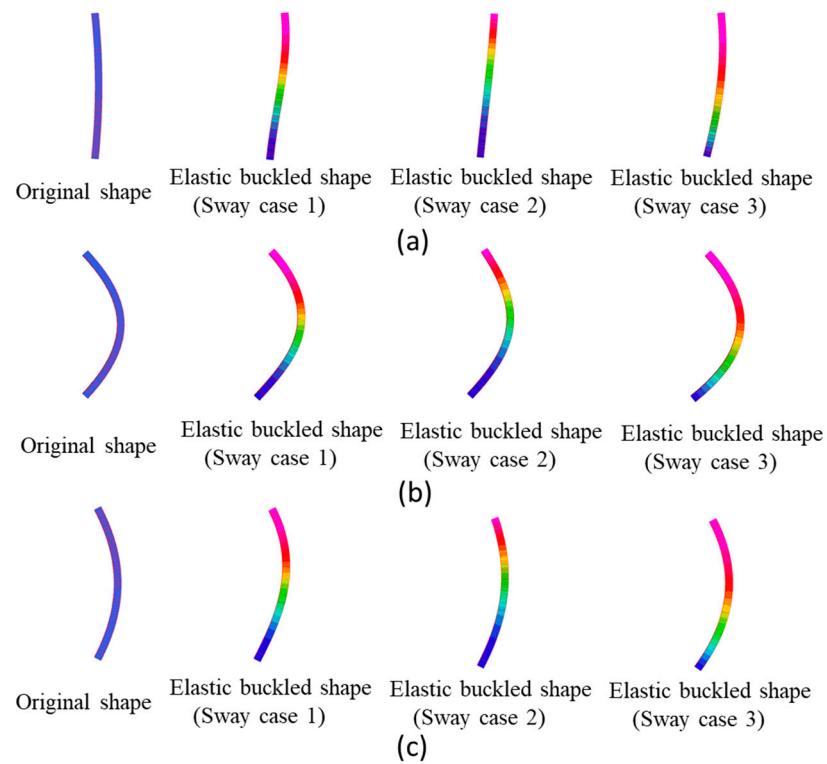


**Figure 21.** (a) The critical elastic buckled shape for the curved column with L/R ratio 0.4; (b) the critical elastic buckled shape for the curved column with L/R ratio 1.0; (c) the critical elastic buckled shape for the curved column with L/R ratio 1.8.

Considering the structural analysis results in Sections 5.1.1 and 5.1.2, the new effective length factors for curved columns under different boundary conditions are summarized in Figure 22.

	Braced member			Sway member		
Buckled shape						
Effective length factor ( $k_e$ )	0.7	0.85	1.2	1.5	2.5	2.5
Note: This table is valid when the L/R ratio is between 0 and 2						

**Figure 22.** The proposed effective length factor for curved members.

### 5.2. Interaction Curves of Perimeter Beams with Different L/R Ratio

After investigating the buckling behavior of the longitudinal column, the buckling behavior of the perimeter beam was investigated to optimize the design of the perimeter beam. In the designed structure, the perimeter beam was mainly subjected to the combined effect of axial load and in-plane bending. Therefore, the interaction curve of the perimeter beam under axial load and bending moment is plotted in this section to determine the impacts of beam curvature on the beam's buckling load capacity.

Four curved beams with different L/R ratios were subjected to the combined effect of axial load and in-plane bending moments, and the results are presented in this section. The dimensions of the four curved beams were all identical: 250 mm × 250 mm × 9 mm. For each beam specimen, eleven combined load cases were applied with a loading factor. Starting from 0, the loading factor kept increasing with an increment of 0.01 until buckling occurred. Before the occurrence of buckling, the maximum loading factor under each combined load case was recorded as the ultimate loading factor for each combined load. Under different load cases, the product of the ultimate loading factor and the applied load was then recorded as the axial load capacity and bending moment capacity of the tested specimen. The obtained axial load capacity and bending moment capacity of beams were normalized using Equations (7) and (8):

$$\text{Normalized compressive capacity} = \frac{N_n}{\phi N_c} \quad (7)$$

$$\text{Normalized bending capacity} = \frac{M_n}{\phi M_{bx}} \quad (8)$$

where  $N_n$  and  $M_n$  are the axial load and bending moment capacity of the tested beam from the numerical analysis, respectively.  $\phi N_c$ ,  $\phi M_{bx}$  are the factorized nominal member capacity and the factorized nominal member moment capacity of the tested beam from AS4100, respectively [8]. For the four curved beams investigated in this section, the diagram of normalized bending capacity versus normalized compressive capacity (interaction curve) is displayed in Figure 23.

Compared with the theoretical interaction curve from AS4100 [8], under pure bending moments, all curved beam specimens exhibited higher bending capacity than the nominal member capacity of beams. With the increase in the applied axial load and the decrease in the applied bending moment, the axial load started to govern the buckling of the beam specimen. For the curved beam with L/R = 0.4, the structural performance under combined load was inferior to the straight beam under the same load when the axial load was greater than  $0.25\phi N_c$ . The curved beam with L/R = 0.8 was more sensitive to axial load when the axial load was greater than  $0.1\phi N_c$ ; the structural performance under combined load was inferior to the straight beam under the same load. The structural performance of the remaining two beams was similar. Both beam specimens exhibited the highest sensitivity to axial load. When the axial load was greater than  $0.05\phi N_c$ , the structural performance under combined load was inferior to the straight beam under the same load. Compared with the straight beam designed according to AS4100 [8], all curved beams in this research demonstrated a higher threshold for the applied bending moment. However, under high axial load, the buckling capacity of all curved beams tended to be less ideal than the straight beam. Hence, when determining the buckling behavior of curved beams, it is improper to use the nominal member capacity of a straight beam in AS4100 [8], because the actual axial load capacity of a curved beam will be significantly lower than the axial load capacity of a straight beam.

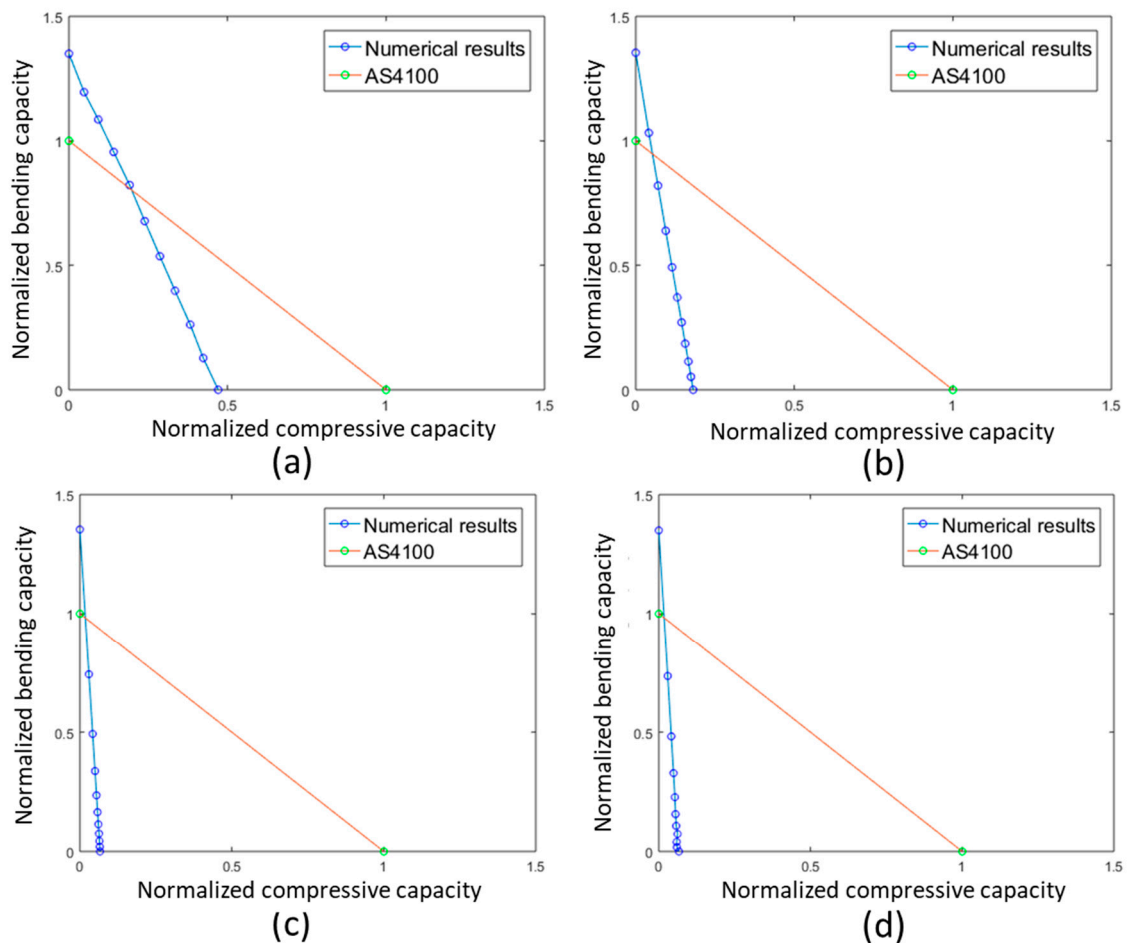


**Figure 23.** Interaction curves of the members with different L/R ratios: (a) for 0.4 L/R ratio; (b) for 0.8 L/R ratio; (c) for 1.2 L/R ratio; (d) for 1.8 L/R ratio.

### 5.3. Possible Buckling Modes of Perimeter Beams at Different Levels

Numerical analysis similar to [42] was conducted to investigate the buckling load and buckling mode of the perimeter beam in the designed structure, and the results are presented in this section. In this case, all numerical models of perimeter beams were developed in ABAQUS using shell elements. As indicated by [43], when a curved beam under a uniformly distributed load is buckled, the beam section will exhibit large displacement near the end connections. To determine the final buckled shape of the curved beam, elastic buckling of the curved beam was analyzed by the finite element software ABAQUS Version 6.14, using the buckle step under the linear perturbation procedure. Six perimeter beams at different levels were selected for study. With the aim of pursuing relatively accurate critical elastic buckling load without excessive computational time, ten buckling modes were requested for each curved beam. The initial reference load subjected to the lateral web of the beam was 1 MPa pressure; the critical buckling load of each buckling mode could be calculated based on the eigenvalue results. The negative eigenvalues (suction effect) were ignored, and only the positive results are plotted in Figure 24.

As shown in Figure 24, the elastic buckling loads varied considerably for each beam. Usually, only the first four minimum local buckling loads need to be considered because the remaining six values are too large, meaning that the corresponding modes are less likely to occur earlier than the previous modes even with imperfections. For the perimeter beams in levels 5, 10 and 15, there were four similar elastic buckling loads corresponding to different local buckling modes, as indicated by the rectangular boxes. This indicates that the curved perimeter beams are very sensitive to imperfections below level 15. The small

imperfections in some directions may create quite different local buckling shapes. However, above level 15, such as levels 20, 25 and 30, there were only two similar buckling loads for the perimeter beams, which implies less uncertainty for prediction of the buckling shape.

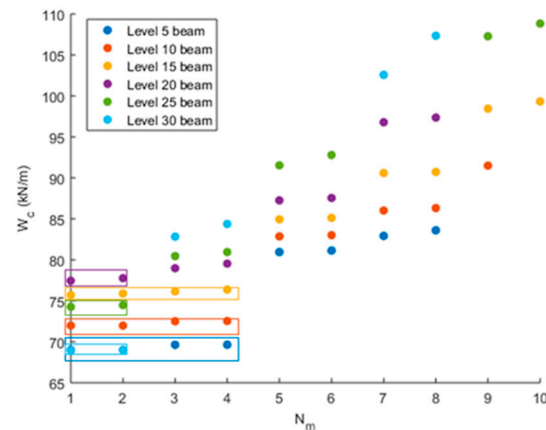


**Figure 24.** The elastic buckling loads ( $W_c$ ) of different modes ( $N_m$ ) for the curved beams on different levels.

As shown in Figure 25, the failure shape of the beam changed greatly in different buckling modes. Compared with the buckling modes for level 5 and level 10 perimeter beams, the buckling shapes always showed asymmetry. In other words, as observed from Figure 25, one end buckled heavily and the other buckled slightly. If only one end was stiffened based on buckling mode 1 to prevent local buckling, it would be a danger because some slight imperfections will bring the beam to another buckling load; the unstiffened end will buckle heavily. The same logic can be applied to level 15 and other level beams, therefore it was necessary to check all possible buckling modes for each perimeter beam instead of only relying on the minimum value. However, in the following sections, it is assumed that the minimum eigenvalue was the critical one when discussing the critical buckling loads because the first few smallest buckling loads are always similar.

#### 5.4. Simulated Buckling Behavior of Perimeter Beams at Different Levels

The buckling loads and buckled shapes of perimeter beams at different levels were determined using ABAQUS. There were a total of 41 levels in the designed steel glass structure. The height from level 0 to level 30 increased gradually, and it decreased gradually from level 31 to level 41. Due to the spindle torus shape, the curvature increased up to level 30 with the increase in the diameter of each level. The middle down-straight section is not supposed to experience significant lateral loads (wind load). Only the elastic buckling behavior perimeter beams between level 0 and level 30 were investigated when the central angles of the perimeter beam were the same (3 degrees from the design schematic) and all perimeter beams were assumed to be the same thin wall section  $RHS\ 250 \times 150 \times 2.0$ .

All of the tests were performed in ABAQUS 6.14 using buckle analysis under linear perturbation module. For simplification, the boundary conditions were assumed to be rigid (rotation fixed) at both ends, although the actual connection is more likely to be semi-rigid. The initial lateral load was set up as a 1 MPa pressure acting on the lateral web. Based on the eigenvalues given by the buckling analysis, the critical buckling load of each perimeter beam could be converted from the pressure to a uniform distributed load (UDL). From the numerical analysis, the results are plotted in Figure 26.

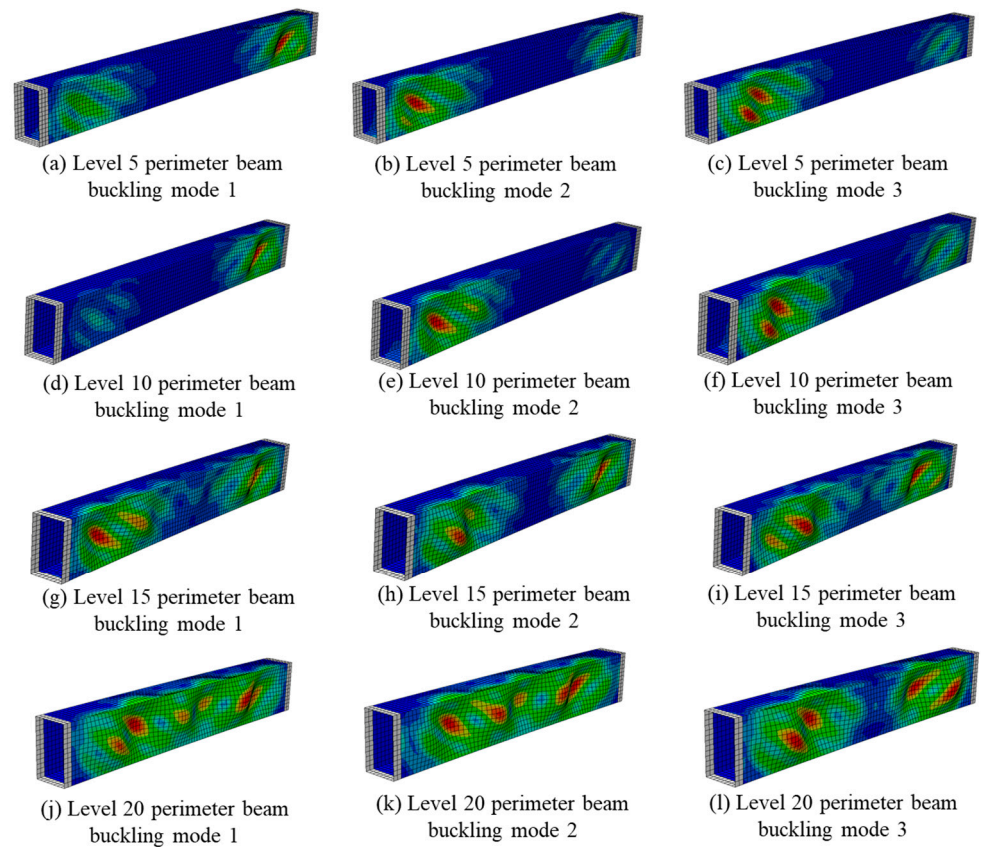


**Figure 25.** The buckling shapes of different modes of each curved beam.

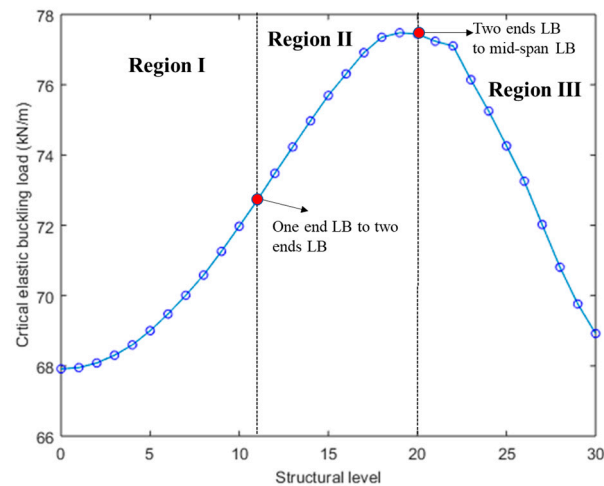


**Figure 26.** The elastic buckling loads ( $W_c$ ) of different structural level (SL) perimeter beams.

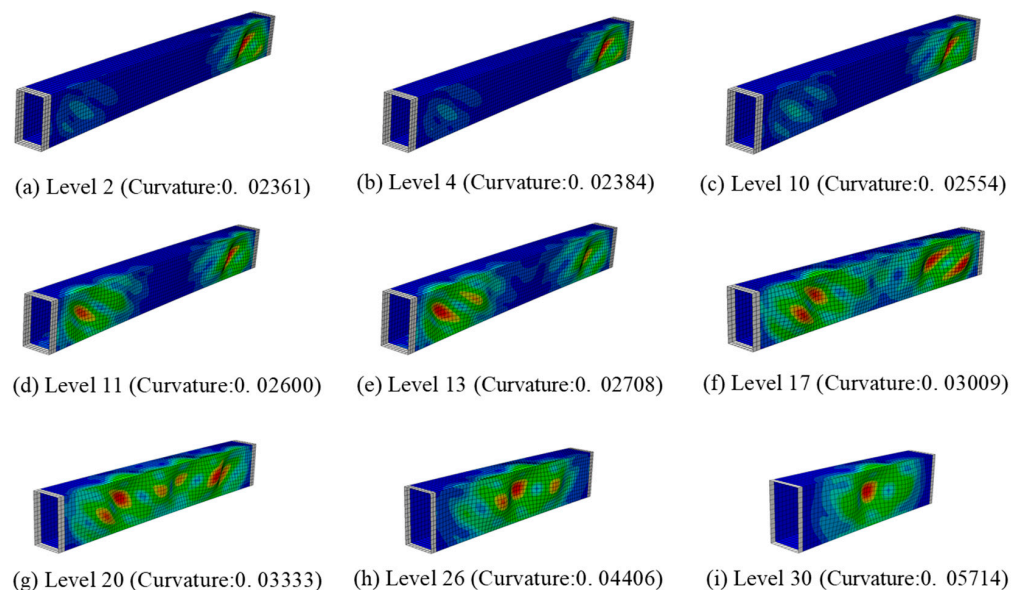
Due to the use of a thin wall section, the buckling mode is governed by the local buckling in all perimeter beams. As shown in Figure 26, the critical elastic buckling load increases from level 0 to level 20 and then it decreases. The maximum buckling load is about 77.44 kN/m around level 20, and the minimum value is approximately 68 kN/m at level 0. The local buckling behavior of the curved perimeter beams can be subdivided into three regions, which are indicated in Figure 26 and Table 15.

**Table 15.** The 3 characteristic local buckling regions.

Regions	Structural Levels	Local Buckling Mode
I	[0–11]	Significant local buckling at one end
II	[11–20]	Significant local buckling at both ends
III	[20–30]	Significant local buckling at the mid-span

In stage I, the local buckling only occurred at one end significantly, whereas the other end experienced slight local buckling, and the mid-span did not experience any failure, which is shown in Figure 27a–c. The local buckling failure mode is axisymmetric in region I. With the increase in the structural level, the curvature increased, but the chord length decreased. When it reached level 11, the local buckling behavior became obvious at both ends, and the overall failure modes were symmetric, as shown in Figure 27d–f. In this region, the local buckling tended to move from both ends to the mid-span with the increase in the structural level. At level 20, the critical elastic buckling mode reached its highest value, and the local buckling started to become more significant at the mid-span rather than the ends. Finally, there was almost no local buckling observed at the ends at level 30.

According to the numerical results from the above analysis, to further improve the lateral load-bearing capacity of the structure, some stiffeners should be added at the ends of some perimeter beams from level 0 to level 20. Particularly, the thicker stiffeners should be added between level 0 to level 11 because the local buckling concentrated only on one end with the smaller critical local buckling loads from level 21 to level 30.

**Figure 27.** The buckling shapes for the perimeter beams with different curvature.

### 5.5. Effects of Boundary Conditions on the Buckling Behavior of Perimeter Beams

Impacts of boundary conditions on the buckling behavior of perimeter beams were investigated using ABAQUS and the results are presented in this section. Numerical analysis similar to [44] was conducted to investigate the buckling behavior of the perimeter beam under different boundary conditions. In this case, all numerical models of the perimeter beam were developed in ABAQUS using shell elements. To obtain representative beam buckling behavior in the proposed design, the perimeter beam at an intermediate level (level 15) was simulated in ABAQUS. According to the original design, the radius of the perimeter beam at level 15 was equal to 35.17 m. The angle between each perimeter beam was equal to  $3^\circ$ . The density and elastic modulus of the perimeter beam were equal to  $7850 \text{ kg/m}^3$  and 200 GPa, respectively. In the original design, the dimensions of the perimeter beam were  $250 \text{ mm} \times 250 \text{ mm} \times 9 \text{ mm}$ . However, according to the buckling

analysis of ABAQUS, the elastic buckling capacity of the original RHS section was fairly large. This indicates the low possibility of elastic buckling. To obtain a more realistic buckling mode and buckling capacity of the perimeter beam, the thickness of the original RHS section was reduced to 2 mm.

In the developed numerical model, both ends of the perimeter beam were partitioned by datum planes. The partitioned ends were set up as two rigid bodies, of which the reference points were located at the centroid of the beam. The initial pressure on the beam's lateral web was set up to 1 MPa. Under ABAQUS buckling analysis, increasing pressure was applied on the lateral web of the perimeter beam until elastic buckling occurred. The developed numerical model considered three types of boundary conditions, which are detailed in Table 16.

**Table 16.** Boundary conditions in the developed numerical model.

Boundary Condition Type	Detailed Boundary Condition
Rigid–Rigid	<ol style="list-style-type: none"> <li>1. Reference point 1: <ul style="list-style-type: none"> <li>- Fixed displacement in <math>x</math>-, <math>y</math>-, <math>z</math>-axes;</li> <li>- Fixed rotation in <math>x</math>-, <math>y</math>-, <math>z</math>-axes.</li> </ul> </li> <li>2. Reference point 2: <ul style="list-style-type: none"> <li>- Fixed displacement in <math>x</math>-, <math>y</math>-, <math>z</math>-axes;</li> <li>- Fixed rotation in <math>x</math>-, <math>y</math>-, <math>z</math>-axes.</li> </ul> </li> </ol>
Rigid–Pinned	<ol style="list-style-type: none"> <li>1. Reference point 1: <ul style="list-style-type: none"> <li>- Fixed displacement in <math>x</math>-, <math>y</math>-, <math>z</math>-axes;</li> <li>- Fixed rotation in <math>x</math>-, <math>y</math>-, <math>z</math>-axes.</li> </ul> </li> <li>2. Reference point 2: <ul style="list-style-type: none"> <li>- Fixed displacement in <math>x</math>-, <math>y</math>-axes, released displacement in <math>z</math>-axis;</li> <li>- Fixed rotation in <math>y</math>-, <math>z</math>-axes, released displacement in <math>x</math>- axis.</li> </ul> </li> </ol>
Pinned–Pinned	<ol style="list-style-type: none"> <li>1. Reference point 1: <ul style="list-style-type: none"> <li>- Fixed displacement in <math>x</math>-, <math>y</math>-, <math>z</math>-axes;</li> <li>- Fixed rotation in <math>y</math>-, <math>z</math>-axes, released displacement in <math>x</math>-axis.</li> </ul> </li> <li>2. Reference point 2: <ul style="list-style-type: none"> <li>- Fixed displacement in <math>x</math>-, <math>y</math>-axes, released displacement in <math>z</math>-axis;</li> <li>- Fixed rotation in <math>y</math>-, <math>z</math>-axes, released displacement in <math>x</math>-axis.</li> </ul> </li> </ol>

Under three different boundary conditions, the buckling modes of the designed structure are demonstrated in Figure 28:

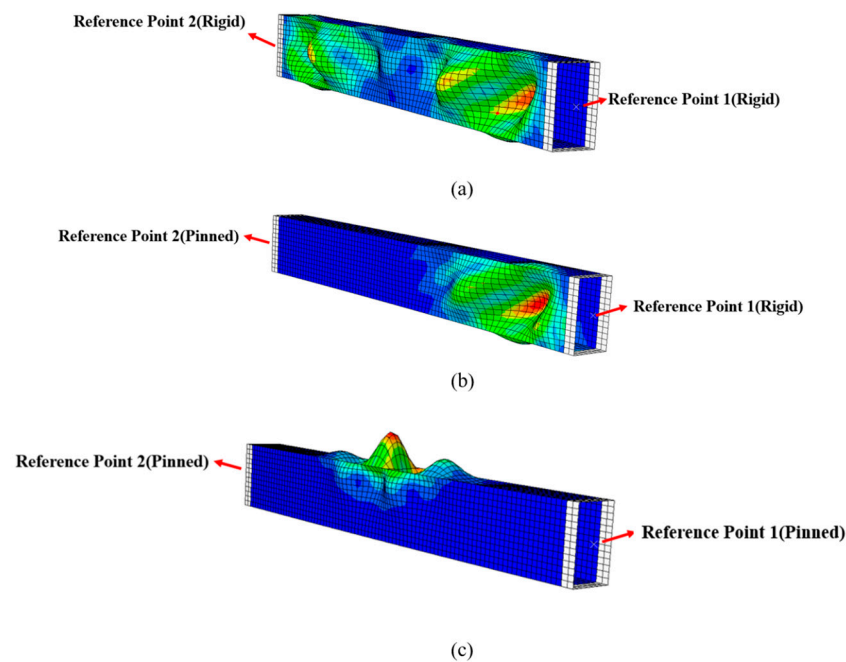


**Figure 28.** (a) Buckling mode of the rigid–rigid perimeter beam; (b) buckling mode of the rigid–pinned perimeter beam; (c) buckling mode of the pinned–pinned perimeter beam.

The buckling capacity of the designed beam was calculated from the eigenvalue of the first buckling mode. In the buckling analysis of ABAQUS, the eigenvalue represents the load factor of the applied load. Therefore, the buckling capacity of the designed beam could be calculated as the product of the eigenvalue and the initial surface pressure. Given the width of the selected beam, the buckling pressure of the beam can then be converted into a line load by:

$$N_{buckle} = P_{buckle} \times w_{beam} \quad (9)$$

Where  $N_{buckle}$  is the critical buckling uniformly distributed load,  $P_{buckle}$  is the corresponding buckling pressure applied on the beam surface,  $w_{beam}$  is the width of the beam surface subjected to uniformly distributed loads.

According to the numerical analysis results, the buckling capacity and corresponding buckling modes of the designed beam under different boundary conditions are summarized in Table 17.

**Table 17.** Buckling capacity and corresponding buckling modes under different boundary conditions.

Boundary Condition	Buckling Capacity (kN/m)	Buckling Failure Mode
Rigid–Rigid	75.75	Local buckling at both fixed
Rigid–Pinned	63.60	Local buckling at the fixed end (reference point 1)
Pinned–Pinned	45.90	Local buckling at the mid-span

As demonstrated in Figure 29, under rigid–rigid boundary conditions, local buckling was observed at both ends of the perimeter beam. Under rigid–pinned boundary conditions, severe local buckling was observed at only the fixed end (reference point). Under pinned–pinned boundary conditions, severe local buckling was observed in the mid-span. The buckling capacities of the perimeter beam under rigid–rigid, rigid–pinned and pinned–pinned conditions were 75.75 kN/m, 63.60 kN/m, and 45.90 kN/m, respectively. With the release of rigid boundary conditions, the buckling capacity of the perimeter beam experienced a significant decrease. This may be ascribed to the concentration of loads within the designed structure. Significant load concentration will induce local buckling, leading to the final structural failure. When the designed beam was fully fixed, the applied

load was concentrated on two fixed ends, which resulted in the highest buckling capacity among three boundary conditions. When the designed beam was only partially fixed, the applied load was concentrated on the only fixed end, which significantly decreased the structural buckling capacity. When the horizontal displacement and in-plane bending were fully released at both ends, the applied load could only concentrate at the mid-span of the beam, which resulted in the lowest buckling capacity among three boundary conditions.

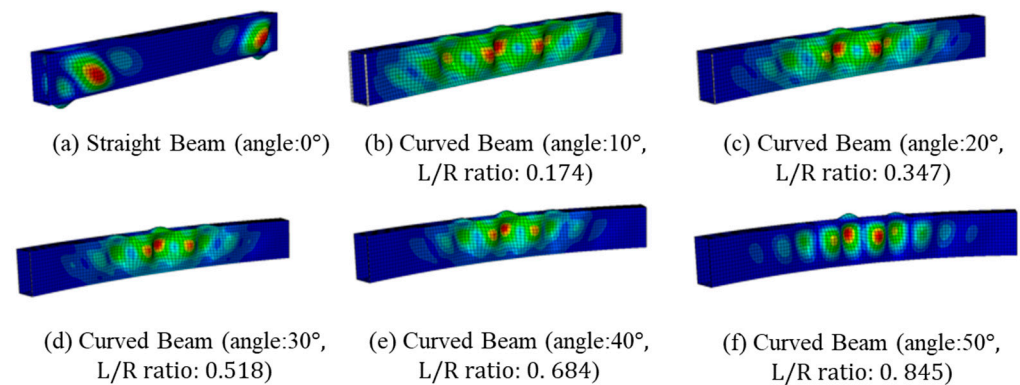


**Figure 29.** Buckling shape of some selected beams.

For the designed spindle torus, the boundary conditions of perimeter beams are hard to determine. Therefore, the designed capacity of perimeter beams was validated using the most pessimistic boundary condition, the pinned–pinned condition. As indicated by the numerical analysis results above, the buckling capacity of a pinned–pinned beam was equal to 45.90 kN/m. According to the calculation in previous sections, the maximum wind load applied on the perimeter beam is only equal to  $-3.615$  kN/m, which is significantly smaller than the buckling capacity of the perimeter beam. Therefore, under the proposed wind load, the structural performance of the designed perimeter beam was satisfied.

#### 5.6. Effects of L/R Ratio on the Buckling Behavior of Perimeter Beams

The impacts of beam curvature on the buckling behavior of the perimeter beam were investigated, and the results are presented in this section. In this case, the L/R ratio acted as a dimensionless parameter which quantified the curvature of the parameter beam. To investigate the impacts of beam curvature (L/R ratio) on the buckling behavior of the perimeter beam, the buckling loads of different curved beam L/R ratios were investigated using ABAQUS. In the numerical analysis, a perfectly straight beam and several curved beams with different L/R ratios were simulated in ABAQUS. The length of the straight beam and the chord length of all curved beams were both equal to 2 m. The cross-sectional dimensions of all selected beams were 250 mm  $\times$  150 mm  $\times$  2 mm. To obtain a more representative buckling behavior of curved beams, the L/R ratio of all selected beams varied from 0 to 2. When the L/R ratio of the curved beam was equal to 0, the beam was considered perfectly straight.

In this numerical analysis, the developed numerical model was similar to the numerical model in Section 5.5. In the model, both ends of the perimeter beam were partitioned by datum planes. Both partitioned ends were set up as a rigid body, of which the reference point was located at the centroid of the cross-section. Uniform pressure was applied on the beam's lateral web. The initial value of the pressure was set as 1 MPa. With increasing pressure on the lateral web, all selected beams were loaded until the occurrence of buckling. To simplify the numerical analysis process, the boundary condition of the tested beam specimen was assumed to be rigid–rigid. From the ABAQUS buckling analysis, the buckling shapes of some selected beams are displayed in Figure 29.

For a perfectly straight beam, the L/R ratio is assumed to be 0. When a perfectly straight beam is loaded until buckled, local buckling is only observed at two fixed ends. However, when the curved angle of the beam grows above  $10^\circ$ , local buckling at the

mid-span will start to dominate the beam buckling mode. With the increase in L/R ratio, the buckling mode of the perimeter beam will experience a gradual change. The increasing L/R ratio will gradually transfer the critical loading point from the fixed end to the mid-span, resulting in variation of the buckling capacity. For the designed perimeter beam, the buckling capacity of beams is interrelated with the beam curvature. To determine the impact of curvature on the buckling capacity of beams, the buckling capacity ratio of curved and straight beams is plotted versus the L/R ratios (curvature) of the curved beams, which is shown in Figure 30.

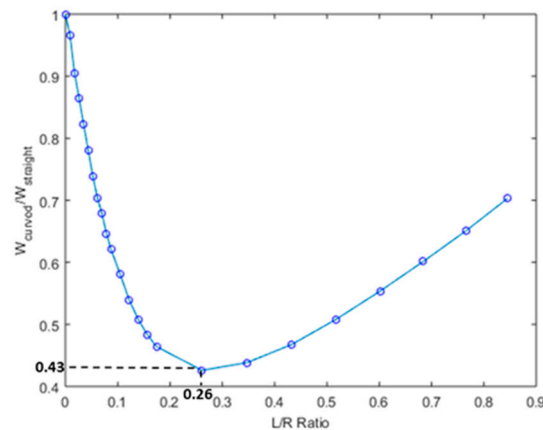


**Figure 30.** The buckling capacity ratio of curved members with different L/R ratios.

For all selected perimeter beams with the same chord length (2 m), the buckling capacity of the beam varied with the beam L/R ratio (curvature). When the L/R ratio (curvature) of the beam was equal to 0, the selected beam was regarded as a perfectly straight beam. In this case, the load capacity of the selected beam was equal to the load capacity of a 2 m straight beam. With the increase in the beam's curvature (L/R ratio), the load capacity of the beam gradually decreased. When the L/R ratio of the beam reached 0.26, the curved member exhibited the lowest buckling load capacity, which was only 43% of the buckling load of a perfectly straight beam.

However, when the L/R ratio of the perimeter beam was greater than 0.26, the buckling capacity of the beam was gradually restored with the increase in the L/R ratio. For all selected beams in this research, the maximum buckling capacity of beams was observed in the straight beam. The minimum buckling capacity of beams was observed in the curved beam with an L/R ratio of 0.26. When the L/R ratio of the curved beam was close to 0, the buckling load capacity of the curved beam was close to the buckling capacity of the straight beam. As suggested by the numerical analysis results, when designing a perimeter beam with a chord length of 2 m, it is essential to prevent the use of beam L/R ratios around 0.26, because the buckling capacity of the perimeter beam is significantly weakened under this L/R ratio.

## 6. Conclusions

### 6.1. Main Findings

Overall, through numerical modeling in Strand7, the proposed spindle torus structure in this paper performed very well under both strength limit states and serviceability limit states. For the strength limit state, under the load combination 1.2G + 1.5Q and 1.35G, the maximum fiber stresses and the maximum load increments between straight member structures and curved member structures were the almost same. However, the curved member structure displayed much lower load-bearing capacity than the straight member structure under the load combination 1.2G + W.

The key load in the strength limit state was the wind load, which was subjected in the plane of curvature rather than outwards, whereas the downward loads, such as dead

load and live load, only had a small influence. Under both load cases in the serviceability limit state, the structural displacement was always governed by the gravity load, and the maximum total displacement was always observed at the central opening.

As indicated above, it was determined that curved member structures do perform differently from straight member structures. Additionally, the SHS sections 9 mm in thickness, which were adopted from the global structural designs, led to very strong strength of the steel members. However, this may be not economical. In the actual design, it is expected to use a combination of 9 mm and 2 mm curved steel members. The behaviors of the curved steel members with 2 mm thickness were studied in both Strand7 and ABAQUS software.

Under both sway and braced boundary conditions, the effective length factor of beams will always increase with the increase in beam curvature (L/R ratio). Additionally, the effective length factor of the curved member under pinned–pinned connection will always be higher than the theoretical effective length factor of the straight member in AS4100 [8]. For perimeter beams at level 5, level 10, and level 15, the buckling load of the first four buckling modes are similar, whereas only the buckling load of the first two buckling modes are similar for perimeter beams at level 20, level 25, and level 30, indicating less uncertainty for member buckling of beams over level 20.

The local elastic buckling is more critical than the overall buckling when analyzing real scale curved members in the proposed design. Regular local buckling locations could be observed in the numerical analysis. Significant local buckling occurred at one end below level 11. Between level 11 and level 20, local buckling happened at both ends significantly. Above level 20, significant local buckling occurred at the mid-span.

## 6.2. Recommendations

Following are some recommendations provided to improve global structure behavior of the proposed spindle torus structure studied in this paper. To reduce the impact of wind loads, it is recommended to use straight members rather than curved members near the central opening, because the top of the structure will tend to withstand greater wind loads in reality. At the same time, it is suggested to design the structure with fewer perimeter beams and longitudinal columns. To reduce the total displacement induced by gravitational load, some vertical columns should be added at the central opening.

Regarding the recommendations for the structural design involving curved steel members, the combined action strength should be analyzed individually in FEM software rather than by simply relying on the results from AS4100 [8] for the curved members with significant axial loads. For the curved members with significant axial loads, combined action strength should be analyzed individually in FEM software rather than simply relying on the results from AS4100 [8]. This is suggested to improve the rigidity of connections between perimeter beams and to avoid pinned–pinned connections between perimeter beams. When designing a perimeter beam with a chord length of 2 m, it is essential to prevent situations of beam L/R ratios around 0.26, because the buckling capacity of a perimeter beam is significantly weakened in this L/R ratio.

## 6.3. Further Research

Although a number of findings and recommendations about spindle torus structure designs are proposed in this paper, there are still some other aspects that could be improved in further study. Firstly, the difference between load-bearing capacities of straight member structures and curved member structures under cyclic loading conditions should be explored. Secondly, new interaction curves regarding curved members with different L/R ratios is proposed as a subject for further research. Thirdly, the most effective thickness and size of the stiffener to prevent local buckling could be explored in future research. Finally, structural performance of the designed structure under serviceability limit state with vertical supports configured in the central opening could be further investigated.

**Author Contributions:** Conceptualization, F.T., Y.W., S.W., S.M.E.S. and F.A.M.; methodology, F.T., Y.W., S.W., J.H., W.S. and F.A.M.; software, F.T., Y.W., S.W., J.H., W.S. and F.A.M.; validation, F.T., Y.W., S.W., J.H. and W.S.; formal analysis, F.T., Y.W., S.W., J.H. and W.S.; investigation, F.T., Y.W., S.W., J.H. and W.S.; resources, F.T., Y.W., S.W., J.H., W.S., H.M., S.M.E.S. and F.A.M.; writing—original draft preparation, Y.W., S.W., J.H. and W.S.; writing—review and editing, F.T., S.M.E.S., H.M. and F.A.M.; visualization, F.T., Y.W., S.W., J.H., W.S. and H.M.; supervision, F.T. and F.A.M.; project administration, F.T. All authors have read and agreed to the published version of the manuscript.

**Funding:** This research received no external funding.

**Institutional Review Board Statement:** Not applicable.

**Informed Consent Statement:** Not applicable.

**Acknowledgments:** The original draft of this paper was the report of the final project of the unit of study CIVL5458 *Numerical methods in civil engineering* at the University of Sydney. The numerical modelling work in this study was carried out in the Hawkins Computer Laboratory in the School of Civil Engineering at the University of Sydney.

**Conflicts of Interest:** The authors declare no conflict of interest.

## References

1. Abeln, B.; Preckwinkel, E.; Yandzio, E.; Heywood, M.; Eliášová, M.; Netušil, M.; Grenier, C. *Development Of Innovative Steel-Glass Structures in Respect to Structural and Architectural Design (Innoglast)*; Publications Office: Luxembourg, 2013.
2. Kido, E.; Cywiński, Z. The new steel-glass architecture of buildings in Japan. *Steel Constr.* **2013**, *6*, 229–237. [[CrossRef](#)]
3. Rykalová, E.; Machovčáková, E. Analysis of Glass Elements Fasted into the Steel Frame. *Appl. Mech. Mater.* **2013**, *351–352*, 208–212. [[CrossRef](#)]
4. Pariafsai, F. A review of design considerations in glass buildings. *Front. Arch. Res.* **2016**, *5*, 171–193. [[CrossRef](#)]
5. Neugebauer, J. Applications for curved glass in buildings. *J. Facade Des. Eng.* **2014**, *2*, 67–83. [[CrossRef](#)]
6. Klyuchnikova, N.V.; Lymar', E.A. The Effect of Metal Filler on Structure Formation of Composite Materials. *Glas. Ceram.* **2005**, *62*, 319–320. [[CrossRef](#)]
7. Zeinoddini, M.; Parke, G.; Disney, P. The Stability Study of an Innovative Steel Dome. *Int. J. Space Struct.* **2004**, *19*, 109–125. [[CrossRef](#)]
8. *AS 4100-1998/Amdt 1-2012: Steel Structures*; Standards Australia International: Sydney, Australia, 2012.
9. King, C.; Brown, D. *Design of Curved Steel*; Steel Construction Institute: Ascot, UK, 2001.
10. Adriaenssens, S.; Ney, L.; Bodarwe, E.; Williams, C. Finding the Form of an Irregular Meshed Steel and Glass Shell Based on Construction Constraints. *J. Arch. Eng.* **2012**, *18*, 206–213. [[CrossRef](#)]
11. Richter, C.; Abeln, B.; Gefßler, A.; Feldmann, M. Structural steel–glass facade panels with multi-side bonding–Nonlinear stress–strain behaviour under complex loading situations. *Int. J. Adhes. Adhes.* **2014**, *55*, 18–28. [[CrossRef](#)]
12. Hoffmeister, B.; Di Biase, P.; Richter, C.; Feldmann, M. Innovative steel-glass components for high-performance building skins: Testing of full-scale prototypes. *Glas. Struct. Eng.* **2016**, *2*, 57–78. [[CrossRef](#)]
13. Weller, B.; Nicklisch, F. Bonding of Glass—Latest Trends and Research. *Struct. Congr.* **2010**, 2545–2554. [[CrossRef](#)]
14. Bennisson, S.J. *Structural Performance of Laminated Glass Made with a “Stiff” Interlayer*; Block, V., Ed.; ASTM International: West Conshohocken, PA, USA, 2002; pp. 57–65.
15. Haarhuis, K.; Wever, T. Glass-reinforced steel structures. *Glas. Struct. Eng.* **2016**, *1*, 195–203. [[CrossRef](#)]
16. Bedon, C.; Zhang, X.; Santos, F.; Honfi, D.; Kozłowski, M.; Arrigoni, M.; Figuli, L.; Lange, D. Performance of structural glass facades under extreme loads—Design methods, existing research, current issues and trends. *Constr. Build. Mater.* **2018**, *163*, 921–937. [[CrossRef](#)]
17. Stoykov, S. Buckling analysis of geometrically nonlinear curved beams. *J. Comput. Appl. Math.* **2018**, *340*, 653–663. [[CrossRef](#)]
18. Park, N.-H.; Choi, Y.-J.; Kang, Y.-J. Spacing of intermediate diaphragms in horizontally curved steel box girder bridges. *Finite Elem. Anal. Des.* **2005**, *41*, 925–943. [[CrossRef](#)]
19. Liu, Y. Crashworthiness design of thin-walled curved beams with box and channel cross sections. *Int. J. Crashworthiness* **2010**, *15*, 413–423. [[CrossRef](#)]
20. Kang, Y.J.; Yoo, C.H. Thin-Walled Curved Beams. I: Formulation of Nonlinear Equations. *J. Eng. Mech.* **1994**, *120*, 2072–2101. [[CrossRef](#)]
21. Yang, Y.; Kuo, S.; Cherng, Y. Curved Beam Elements for Nonlinear Analysis. *J. Eng. Mech.* **1989**, *115*, 840–855. [[CrossRef](#)]
22. Timoshenko, S.; Gere, J.M. *Theory of Elastic Stability*, 2nd ed.; McGraw-Hill: New York, NY, USA, 1961.
23. Kuo, S.; Yang, Y. New Theory on Buckling of Curved Beams. *J. Eng. Mech.* **1991**, *117*, 1698–1717. [[CrossRef](#)]
24. Firmo, F.; Jordão, S.; Neves, L.C.; Bedon, C. Exploratory study on simple hybrid or pre-stressed steel-glass I-beams under short-term bending—Part 1: Experiments. *Compos. Struct.* **2020**, *234*, 111651. [[CrossRef](#)]

25. Gatheeshgar, P.; Poologanathan, K.; Gunalan, S.; Nagaratnam, B.; Tsavdaridis, K.D.; Ye, J. Structural behaviour of optimized cold-formed steel beams. *Steel Constr.* **2020**, *13*, 294–304. [[CrossRef](#)]
26. Buchanan, C.; Zhao, O.; Real, E.; Gardner, L. Cold-formed stainless steel CHS beam-columns—Testing, simulation and design. *Eng. Struct.* **2020**, *213*, 110270. [[CrossRef](#)]
27. Zhang, C.; Wang, Q. Free vibration analysis of elastically restrained functionally graded curved beams based on the Mori–Tanaka scheme. *Mech. Adv. Mater. Struct.* **2018**, *26*, 1821–1831. [[CrossRef](#)]
28. Yan, C.; Wang, Y.; Zhai, X.; Meng, L. Strength assessment of curved steel-concrete-steel sandwich shells with bolt connectors under concentrated load. *Eng. Struct.* **2020**, *212*, 110465. [[CrossRef](#)]
29. Woon, W. *Changi Airport as Landscape for Nation-Building*; National University of Singapore: Singapore, 2015.
30. Pak, J.K. *A Detailed Analysis and Design for Future Proofing Singapore's Changi Airport*; University of Hawai'i at Manoa: Honolulu, HI, USA, 2017.
31. AS/NZS 1170.1:2002 (Including Amendments Nos.1 and 2). *Structural Design Actions. Part 1: Permanent, Imposed and Other Actions*; Standards Australia International: Sydney, Australia, 2009.
32. AS/NZS 4600: *Cold-Formed Steel Structures*; Standards Australia International: Sydney, Australia, 2018.
33. *Onesteel Manufacture Guide*; Onesteel Manufacturing Pty Limited: Sydney, Australia, 2008.
34. AS/NZS 1170.2:2011 (Including Amendments Nos.1 and 2). *Structural Design Actions. Part 2: Wind Actions*; Standards Australia International: Sydney, Australia, 2012.
35. *Eurocode 1: Actions on Structures—Part 1–4: General Actions—Wind Actions*; CEN: Brussels, Belgium, 2005.
36. AS/NZS 1170.0:2002 (Including Amendments Nos.1,2,4 and 5). *Structural Design Actions. Part 0: General Principles*; Standards Australia International: Sydney, Australia, 2011.
37. Kliem, B.; Török, T. Torus Instability. *Phys. Rev. Lett.* **2006**, *96*, 255002. [[CrossRef](#)] [[PubMed](#)]
38. Zhao, X.-L.; Wilkinson, T.; Hancock, G. *Cold-Formed Tubular Members and Connections*; Elsevier BV: Amsterdam, The Netherlands, 2005.
39. Rajan, S. *Introduction to Structural Analysis & Design*; John Wiley: New York, NY, USA, 2000.
40. González, C.; Llorca, J. Stiffness of a curved beam subjected to axial load and large displacements. *Int. J. Solids Struct.* **2005**, *42*, 1537–1545. [[CrossRef](#)]
41. Trahair, N.; Papangelis, J. Lateral-distortional buckling of beams with hollow flanges and folded plate webs. *Eng. Struct.* **2018**, *163*, 71–76. [[CrossRef](#)]
42. Kankanamge, N.D.; Mahendran, M. Behaviour and design of cold-formed steel beams subject to lateral–torsional buckling at elevated temperatures. *Thin-Walled Struct.* **2012**, *61*, 213–228. [[CrossRef](#)]
43. Zare, M.; Asnafi, A. Nonlinear pre and post-buckled analysis of curved beams using differential quadrature element method. *Int. J. Mech. Mater. Eng.* **2019**, *14*, 15. [[CrossRef](#)]
44. Chu, X.T.; Ye, Z.M.; Kettle, R.; Li, L.Y. Buckling behaviour of cold-formed channel sections under uniformly distributed loads. *Thin-Walled Struct.* **2005**, *43*, 531–542. [[CrossRef](#)]